Plasma Photocathodes

Ahmad Fahim Habib,* Thomas Heinemann,* Grace G. Manahan, Daniel Ullmann, Paul Scherkl, Alexander Knetsch, Andrew Sutherland, Andrew Beaton, David Campbell, Lorne Rutherford, Lewis Boulton, Alastair Nutter, Adam Hewitt, Alexander Dickson, Oliver S. Karger, Michael D. Litos, Brendon D. O'Shea, Gerard Andonian, David L. Bruhwiler, Georg Pretzler, Thomas Wilson, Zhengming Sheng, Michael Stumpf, Lars Reichwein, Alexander Pukhov, John R. Cary, Mark J. Hogan, Vitaly Yakimenko, James B. Rosenzweig, and Bernhard Hidding*

Plasma wakefield accelerators offer accelerating and focusing electric fields three to four orders of magnitude larger than state-of-the-art radiofrequency cavity-based accelerators. Plasma photocathodes can release ultracold electron populations within such plasma waves and thus open a path toward tunable production of well-defined, compact electron beams with normalized emittance and brightness many orders of magnitude better than state-of-the-art. Such beams will have far-reaching impact for applications such as light sources, but also open up new vistas on high energy and high field physics. This paper reviews the innovation of plasma photocathodes, and reports on the experimental progress, challenges, and future prospects of the approach. Details of the proof-of-concept demonstration of a plasma photocathode in 90° geometry at SLAC FACET within the E-210: Trojan Horse program are described. Using this experience, alongside theoretical and simulation-supported advances, an outlook is given on future realizations of plasma photocathodes such as the upcoming E-310: Trojan Horse-II program at FACET-II with prospects toward excellent witness beam parameter quality, tunability, and stability. Future installations of plasma photocathodes also at compact, hybrid plasma wakefield accelerators, will then boost capacities and open up novel capabilities for experiments at the forefront of interaction of high brightness electron and photon beams.

1. Introduction

In 1887, Hertz discovered the photoelectric effect when experimenting with the generation of radiowaves.[1] Einstein's explanation of this effect[2] and the quantum theory of radiation[3] were foundational contributions for quantum and atomic physics, and the realization of the laser.[4] At the same time, particle accelerators were developed that allowed production of increasingly intense and energetic beams to investigate atomic and sub-atomic structures and processes. Prominently, the photoelectric effect is exploited in the photocathodes of modern linear accelerators, where typically infrared but then frequency-upconverted laser pulses release bursts of electrons from suitable photocathode materials. These electrons are then captured and accelerated by high-frequency radiowaves in accelerator cavities. This technologically advanced combination of Einstein's photoelectric effect and the laser, and Hertz' radiowaves, is a foundation for

A. F. Habib, T. Heinemann, G. G. Manahan, D. Ullmann, A. Sutherland, A. Beaton, D. Campbell, L. Rutherford, L. Boulton, A. Nutter, A. Hewitt, A. Dickson, T. Wilson, B. Hidding
Scottish Universities Physics Alliance, Department of Physics
University of Strathclyde
Glasgow, UK
E-mail: ahmad.habib@strath.ac.uk; thomas.heinemann@strath.ac.uk; bernhard.hidding@strath.ac.uk

A. F. Habib, T. Heinemann, G. G. Manahan, D. Ullmann, A. Sutherland, A. Beaton, D. Campbell, L. Rutherford, L. Boulton, A. Nutter, A. Hewitt, A. Dickson, T. Wilson, B. Hidding
Cockcroft Institute, Sci-Tech Daresbury
Daresbury, Cheshire, UK

P. Scherkl
University Medical Center Hamburg-Eppendorf: Universitätsklinikum Hamburg-Eppendorf
Martinistr. 52, 37734 Hamburg, Germany

A. Knetsch
LOA, ENSTA Paris, CNRS, Ecole Polytechnique
Institut Polytechnique de Paris
91762 Palaiseau, France

O. S. Karger
OHB System AG
Universitätsallee 27, Bremen, Germany

**ADVANCED
SCIENCE NEWS**

www.advancedsciencenews.com

*annalen
der* **physik**

www.ann-phys.org

the production of intense electron beams in today's particle accelerators.

These electron beams in turn power, for example, high-energy particle colliders, synchrotron radiation facilities and X-ray free-electron lasers (X-FELs), and thus enable groundbreaking discoveries in fundamental physics, material, and life sciences. For all these applications, electron beams that are compact in 6D phase space are required. A compound figure of merit that quantifies beam quality is the beam brightness, either in the form of the 5D brightness $B_{5D} = 2I/\epsilon_n^2$, where I and ϵ_n are the beam current and the transverse normalized emittance, respectively, or the 6D brightness $B_{6D} = B_{5D}/0.1\% \Delta W/W$, which in addition takes into account the energy spread, where ΔW is the r.m.s energy deviation and W is the average electron energy of the beam.

Photocathode-based electron guns capable of generating high-brightness beams enabled, for example, the demonstration of the first X-ray free-electron laser, the Linear Coherent Light Source (LCLS)[5,6] at the SLAC National Accelerator Laboratory. In the electron gun, the interplay of laser parameters and cathode material determines the residual transverse momenta of the emitted electrons and thus defines the initial emittance of the released electron population.[7,8] To minimize subsequent space charge induced emittance growth, rapid acceleration immediately after emission is required[8] to produce high-brightness beams. However, the extraction and acceleration fields in electron guns and linacs based on radio frequency (RF) metallic cavities are normally constrained to some tens of MV m^{-1} up to about 100 MV m^{-1}, due to material integrity limits of the ac-

M. D. Litos
Center for Integrated Plasma Studies, Department of Physics
University of Colorado
Boulder, CO, USA

B. D. O'Shea, M. J. Hogan, V. Yakimenko
SLAC National Accelerator Laboratory
Menlo Park, CA, USA

G. Andonian
Radiabeam Technologies
Santa Monica, CA 90404, USA

D. L. Bruhwiler
RadiaSoft LLC
Boulder, CO 80301, USA

G. Pretzler, M. Stumpf
Institut für Laser- und Plasmaphysik
Heinrich-Heine-Universität Düsseldorf
40225 Düsseldorf, Germany

Z. Sheng
Key Laboratory for Laser Plasmas (MoE), School of Physics and Astronomy
Shanghai Jiao Tong University
Shanghai 200240, China

L. Reichwein, A. Pukhov
Institut für Theoretische Physik I
Heinrich-Heine-Universität Düsseldorf
40225 Düsseldorf, Germany

J. R. Cary
Tech-X Corporation
Boulder, CO, USA

J. B. Rosenzweig
Department of Physics and Astronomy
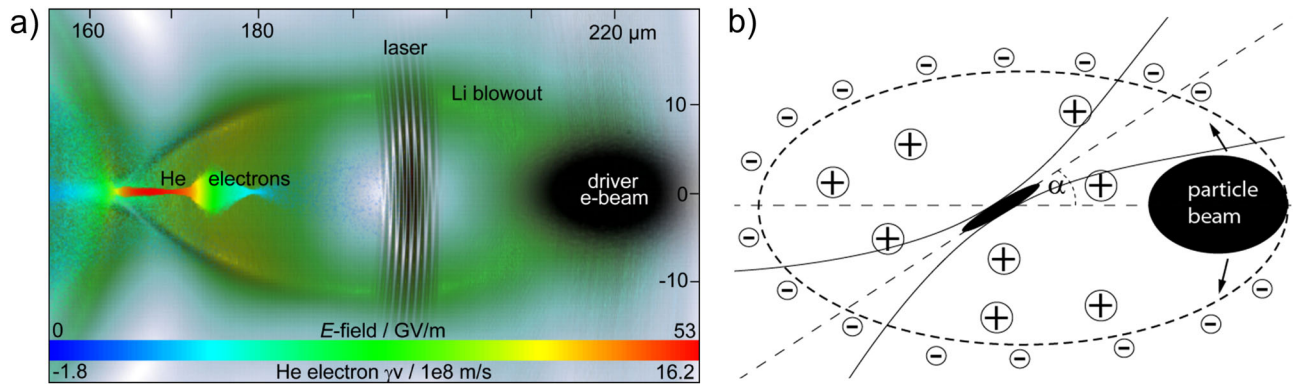University of California Los Angeles
Los Angeles, CA, USA

celerator building blocks. The initial electron beam typically has picosecond-level duration and up to tens of Ampere current, as a trade-off aiming for low residual emittance while operating at the photocathode gun limits.[9] Multi-stage compression techniques are afterward required to reduce the duration of the produced electron beams to as short as a few tens of femtoseconds for kA beam currents. However, electron beams are meanwhile subject to coherent synchrotron radiation (CSR) in the dispersive beam compressors, known to induce energy and density modulations along the electron bunch. These microbunching instabilities have a detrimental impact on the obtainable final beam emittance and brightness.[10–12]

Summarizing, the generation and acceleration of low emittance, short-pulse, high-brightness electron beams in conventional linacs is a great success story, but the generation of beams beyond the state-of-the-art of currents of kA-scale and normalized emittances of mm-mrad scale faces a number of challenges and limitations. Due to the importance of electron beam brightness and emittance, for example, for FELs,[13] novel approaches that seek to decrease the residual momentum spread and increase the accelerating field, such as high-field cryogenic photoelectron guns, are investigated.[14] Another approach that can achieve high-brightness beams is the interaction of low-power laser pulses with nanophotonic structures, albeit particularly suitable for the fC-charge regime.[15]

Plasma-based accelerators are fundamentally different to classical accelerators. In this approach, the accelerating gradient is not limited by the material integrity threshold of the rf-cavities. Instead, matter is purposefully broken down into ions and electrons, and transient collective charge separation, driven by intense laser pulses[16] or intense electron beams[17] generates a plasma wave in the wake of the driver. The driver's function is to expel plasma electrons transversally out of its path, while the heavier, quasi-stationary plasma ions then collectively re-attract these electrons and thus form a co-propagating plasma wave cavity that is void of electrons, known as the blowout regime.[18] The frequency ω_p of this plasma wave oscillation, the corresponding plasma cavity length λ_p, and the transverse and longitudinal electric fields inside this plasma wave, are mainly determined by the plasma density n_e. From the collective, transient charge imbalance in these plasma waves an electrostatic field arises, which can be used for acceleration and focusing. The chief attraction of plasma wakefield accelerators are the huge accelerating and focusing electric fields of the order of GV m^{-1} to TV m^{-1} that they can support through these collective oscillations of plasma electrons at plasma densities n_e exceeding $n_e > 10^{15}$ cm^3. Electron-beam driven plasma wakefield accelerators (PWFA) enable not only tens of GeV energy gains of electrons on metre-scale distances,[19,20] but also provide a unique environment to realize plasma-based electron injector guns for generation of ultra-high brightness electron beams.

In this paper, we first introduce plasma photocathodes and advancements in the field, then we discuss and provide new insights into the results obtained within the "E-210: Trojan Horse" experiment at SLAC FACET, which for the first time demonstrated a plasma photocathode injector,[21] in perpendicular injector geometry. Then, optimization for future realizations of plasma photocathodes are discussed, using the "E-310: Trojan Horse-II" successor program at SLAC FACET-II as showcase.

**ADVANCED
SCIENCE NEWS**

www.advancedsciencenews.com

annalen
der **physik**

www.ann-phys.org

Figure 1. a) The plasma photocathode visualization from the original publication,[22] showing the laser-ionized HIT electrons trapped in the electron beam driven LIT-based plasma wake blowout propagating to the right, and b) a drawing from[24] showing that the injection laser angle α can be arbitrary and the effective Rayleigh length may be varied. a) Reproduced with permission.[22] Copyright 2012, American Physical Society.

Based on the lessons learned, and on identified optimization strategies, these will aim at demonstrating the full potential of the capabilities of the plasma photocathode injector toward ultrabright beams. Finally, guided by existing work, we recapitulate the impact of variations of plasma photocathode laser timing, transverse offset and intensity on witness beam parameters around a potential working point as result of shot-to-shot jitters, indicating prospects for remarkable stability of the plasma photocathode beam output. Further, we review beam quality preservation at the nm-rad normalized emittance level and potential application of X-FEL.

2. The Plasma Photocathode

The plasma photocathode,[22] informally also known as Trojan Horse,[23] has been invented[24] to exploit the strong electric fields in plasma not only for acceleration, but also for high-quality bunch generation. In a plasma photocathode, a laser pulse is harnessed to release electrons from a cathode material—as in a classical photogun. It features a high-ionization threshold (HIT) gas component as underdense photocathode medium combined with a background low-ionization threshold (LIT) medium based plasma wave. The tens of GV m^{-1} extraction fields of the plasma wave at the same time also act as bunch compressor, in the pre-ionized LIT medium.

Figure 1 shows the principle as visualized in the original publication[22] in Figure a, and by one of the drawings used in the underlying patent.[24] The electron (or more generally, particle) beam excites a plasma wave based on the LIT medium, and the laser pulse releases plasma electrons in its focus from HIT component ionization directly within the plasma wave either in collinear geometry (Figure 1a) or, more generally, at arbitrary relative propagation angle (Figure 1b).

Key differences to a classical photocathode/photogun are that i) the electrons are produced directly inside the accelerating structure, where they are immediately subject to tens of GV m^{-1}-scale accelerating and focusing electric fields, ii) the electrons are obtained from tunneling ionization of a higher ionization threshold medium instead of single or multi-photon ionization, and iii) the releasing laser pulse propagates through underdense plasma, in contrast to the laser-solid interaction in conventional photocathodes. The plasma photocathode injector is largely decoupled from the plasma wakefield, and allows releasing plasma electrons at arbitrary positions within the plasma wave, as well as various laser pulse geometries and angles.[24] Thereby, the electron beam charge, duration and current distribution can be tuned, similarly to conventional photocathodes. Plasma photocathodes, therefore, offer a large degree of flexibility for electron beam production, but most fundamentally and importantly, a path toward ultra-low emittance and ultra-high brightness electron beams. This is because i) the electrons, being released by laser intensities just above the tunnel ionization threshold, are initially ultra-cold with very small residual momentum and thus minimized thermal emittance, ii) are released in a small transverse volume, iii) space-charge induced emittance growth is strongly suppressed by the rapid acceleration to relativistic energies, and iv) phase-mixing is very small due to the localized release volume. At the same time, velocity bunching[25] of the electrons to fs or even sub-fs duration in the accelerating plasma cavity with a size of typically a few hundreds of µm, is inherently suitable to produce bunches at kA-level currents. Combined with nm rad-level emittances, this results in beam brightness many orders of magnitude larger than what is feasible with conventional photocathode gun linacs.

For the analysis and development of plasma photoguns, the two components, the plasma photocathode release process itself on the one hand, and the plasma wakefield accelerator process on the other hand, can to some extent be tackled independently from one another. **Figure 2** visualizes the plasma electrons produced from a fully-resolved plasma photocathode laser pulse, based on simulations with the particle-in-cell (PIC) code FBPIC.[26] In this example, a Gaussian Ti:Sapphire laser pulse with wavelength 800 nm, pulse duration $\tau = 50$ fs, an r.m.s spot size $w_0 = 7$ µm and a default focus intensity in terms of the dimensionless laser amplitude $a_0 = eE/(\omega m_e c) = 0.018$ is used, where E is the electric field amplitude and ω is the laser frequency. Helium gas is used as the HIT component at a density of 2.3×10^{17} cm^{-3}. In the simulation, the snapshot shown in Figure 2a is taken after the laser pulse, propagating in the positive z-direction, has finished generating the initial plasma and has just left the simulation box. While in a plasma photocathode embedded into a PWFA, the produced electrons would be accelerated and compressed immediately by
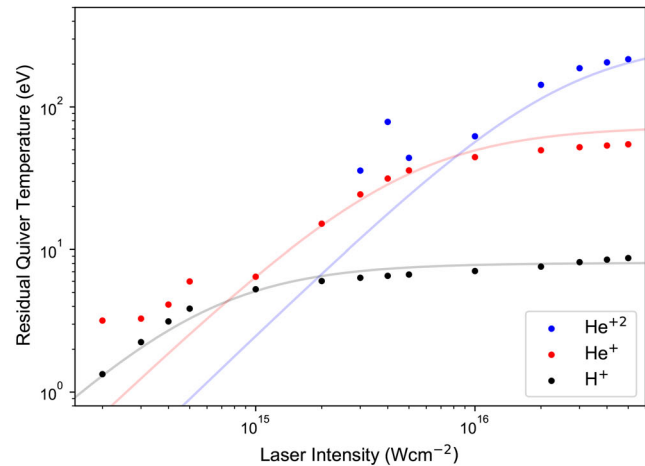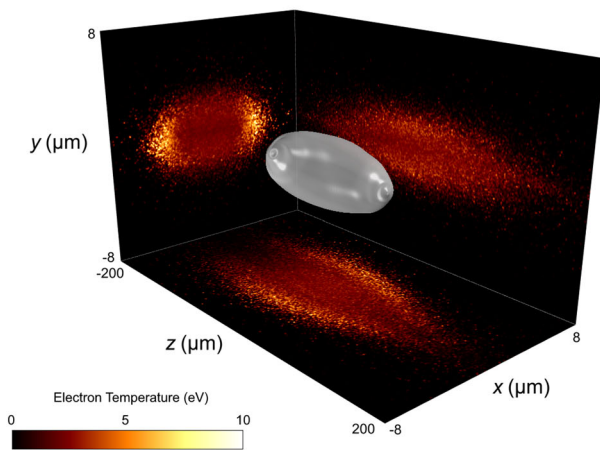
Figure 2. a) The plasma volume and temperature resulting from tunneling ionization by the plasma photocathode laser pulse. The ellipsoid volume is produced by the Gaussian laser pulse, the projections show the resulting electron temperatures shortly after the laser pulse has passed. b) The residual quiver temperatures for several species over a wide range of intensities. The transition between the partially-ionized and saturation regimes is shown by the simulation results (scatter points).

the plasma wave, here the plasma wakefield is not included to allow illustration of the characteristics of the purely photocathode-released electron population without the superimposed acceleration process. Figure 2a shows a 3D visualization of the produced electron density in the centre, represented by the white isosurface plot. The elliptical shape of this ionization volume is the result of the laser intensity profile along its propagation direction, characterized by the Rayleigh length $Z_R = \pi w_0^2/0.8\,\mu m$ and the laser intensity with respect to the tunneling ionization threshold of He. The ionization volume and hence the produced charge can therefore be adjusted by both spot size and laser intensity—or more generally, may be tuned by any interaction parameter that changes local tunneling ionization rates. The projections show associated integrated plasma electron temperatures, calculated by $T \approx 2/3\langle E_k \rangle$, where $\langle E_k \rangle$ is the average kinetic energy of the particles in the projection direction. The electron temperatures near the centre of the plasma photocathode ionization volume are smaller than farther outside the centre. This is a combination of the initial residual momentum[27] distribution of electrons released in the laser field, and the accumulated transverse drift of electrons after being born in the laser field. Hence, as seen in the projections, the plasma in this snapshot is not fully symmetric, but electrons born earlier have travelled further to the outside than electrons born later. In this example, the laser pulse is linearly polarized in the horizontal direction, which is reflected by the projections and their asymmetric shape, due to thermal expansion in the polarization direction. Again, in a plasma photocathode embedded into a suitable plasma wave wakefield, the wakefields would compress the electrons transversally and longitudinally, which would dominate the evolving shape of the accelerated beam. Crucially important is that the resulting electron temperatures are low and of the order of a few eV—the basis for the minimized thermal emittance. The transverse electron beam emittance is collectively determined by the transverse electron positions x, y in space and their corresponding transverse momenta $p_{x,y}$.[28] A compact size in real space, and compact size in

phase space are hence recipes for ultralow emittance. Figure 2a shows that both are naturally provided by a plasma photocathode.

Figure 2b shows computational scans of the residual quiver temperature (ref. [29] Equations 14 and 17) of released electrons versus laser intensity for different HIT components, as obtained by FBPIC. Higher intensities are required for media with higher ionization thresholds, and consequently the corresponding electron temperatures are likewise higher. The residual quiver temperature is associated with the strength of the laser field only at the moment of ionization. Thus, in the regime where only part of the gas is expected to be ionized by the laser, the temperature scales with the peak intensity of the pulse. However, for a laser with a peak intensity greatly exceeding the ionization threshold, it is likely that all electrons will be released by ionization before the peak of the pulse arrives, and therefore the electron temperature plateaus at a saturation value. This saturation value can be estimated numerically by considering the electric field value at which it is very likely an electron will be liberated within one laser cycle. The obtained temperatures are in good agent with thermal emittance calculations (solid lines) from ref. [29], which refined the emittance scaling from.[22] Similar as for conventional photocathodes, where, for example, photocathode material, shape, and laser pulse is varied, a huge range of potential variations exists for plasma photocathodes. The plasma photocathode laser pulse properties and its intensity form factor convoluted with the HIT medium density and profile can be tailored to control the rate of released electrons in space and time. This facilitates precise control over the properties of the trapped electron beams, for example, by using non-Gaussian laser pulse profiles, various focusing optics, laser pulse propagation direction, polarization directions, laser frequencies, or simultaneous spatial and temporal focusing (SSTF) laser pulses[30] or reflection-based plasma photocathode optics for doughnut-shaped laser pulse profiles and tailored ionization volumes.[31]

Figure 3 summarizes the idea of SSTF as investigated in ref. [30], inspired by a suggestion expressed in ref. [32]. As sketched

**ADVANCED
SCIENCE NEWS**

www.advancedsciencenews.com

annalen
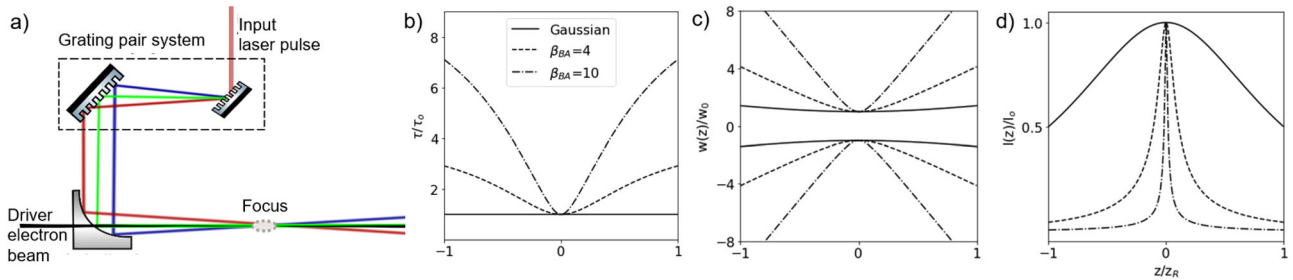der **physik**

www.ann-phys.org

Figure 3. Simultaneous spatial and temporal focusing (SSTF) of plasma photocathode laser pulses. A grating pair generates a transverse spatial frequency chirp, such that the laser pulse individual laser frequencies recombine only at focus, thereby reducing the effective Rayleigh length a). The degree of spatial chirp β_{BA} then determines the compression in time b) and space c) and the laser intensity at focus d).
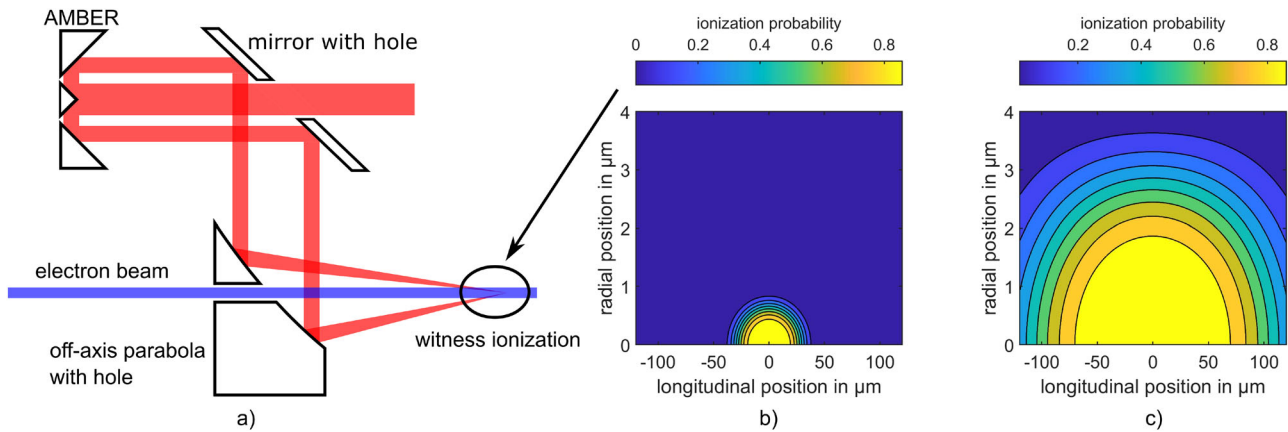

Figure 4. a) Setup for collinear Trojan Horse injection using the optical device AMBER to create a doughnut laser pulse profile as proposed in ref. [31]. b) Tailored ionization profile for Ar^{2+} using the device AMBER. c) Ionization profile for Ar^{2+} by using a Gaussian beam profile. Adapted under the terms of the CC-BY license.[31] Copyright 2022, The Authors, Published by IOP Publishing Ltd.

in Figure 3a, in this industrially-known method a transverse spatial chirp is applied, such that the different laser colors overlap in time (Figure 3b) and space (Figure 3c) only in the focus. Thereby, the pulse becomes broadband and hence short, simultaneously with reaching the geometric focus. As consequence, the intensity peak (Figure 3d) is confined to a much shorter length around axis, which can be adjusted by the degree of spatial chirp β_{BA}.

Another method by which the ionization release volume can be tuned is by generating a doughnut-shaped laser pulse, using a specially designed reflective optics called Axicon Mirror Beam ExpandeR (AMBER) as shown in **Figure 4**a. This setup allows one to reduce the ionization volume as shown in Figure 4b when compared to the ionization volume resulting from the Gaussian pulse as shown in Figure 4c for comparison. The resulting charge yields have been measured in good agreement with predictions in ref. [31].

The flexibility of the plasma photocathode, including, for example, variation of the laser frequency and its impact on the effective ionization volume, contributions by ionization defocusing, the use of multiple laser pulses or arbitrary propagation angles between wake and injector laser(s) had been expressed already in ref. [24], and gives room for permutations of the scheme. For example, in ref. [23, 27, 33] the use of higher frequency laser pulses for injection, its impact on injection (Rayleigh) length, betatron phase mixing, and potential multi-photon ionization issues has been discussed. An alternate scheme using colliding laser pulses

to confine the injection area was presented,[34] and a theoretical laser-driven version of the scheme using higher frequency injector pulses and lower frequency driver lasers was considered[35]— a scheme reminiscent of an idea mentioned in ref. [36]—and the use of two laser pulses at the same frequency, but different a_0 for ionization injection,[32] a scheme similarly recently realized experimentally.[37]

After thermal emittance obtained during electron release by the plasma photocathode laser pulse, emittance contributions due to transverse betatron phase mixing[27,38] set in, and at higher charge levels space charge begins to dominate the obtainable emittance levels. The principal benefit of confined ionization volumes is the reduced emittance contribution from betatron phase-mixing, and may be useful in particular in the low charge regime, where in turn space charge emittance contributions are still low. By taking advantage of multi-bunch injection[39] with multiple plasma photocathode lasers, tunable electron beam chirp control can be performed in the same plasma acceleration stage by the 'escort bunch' beam-loading approach.[40] This allows preservation of ultralow emittance and ultrahigh brightness of a previously generated witness beam. The relative energy spread of the electron beams in this scheme can amount to $\simeq 0.01\%$ at few-GeV energies, thus resulting in ultrahigh 6D brightness.[40]

Experimentally, a sufficiently strong drive beam to excite a strong plasma wave is required. Essentially, the electrostatic potential $\phi(\zeta)$ of the wake, where $\zeta = z - ct$ is the co-moving
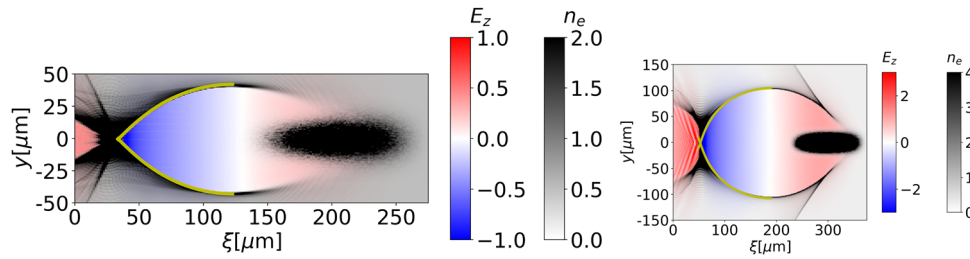
Figure 5. Electrons density and longitudinal electric field for a blowout driven by a 1 GeV electron driver with peak density $3n_{crit}$ (left) and $24n_{crit}$ (right) from PIC simulations (density clipped for better visibility). The yellow lines correspond to the solution of differential Equation (1). Fields are normalized to $m_e c \omega_p / e$ and densities to the critical density n_{crit}; throughout the simulations the plasma wavelength is $\lambda_p = 200$ μm. Reproduced under the terms of the CC-BY license.[52] Copyright 2020, The Authors, published by IOP Publishing Ltd.

coordinate along the propagation axis z, should be large enough to allow capturing of released plasma electrons from rest, after being released by the plasma photocathode laser pulse. For PWFA, this means a driver beam with sufficiently high current and charge density is needed. So far, the only linac in the world with sufficient electron beam current that could be used for PWFA and plasma photocathode realization was SLAC's Facility for Advanced Accelerator Experimental Tests FACET. While linacs such as FACET and FACET-II will remain the gold standard for intense and reliable electron beam production at multi-GeV for some time, hybrid plasma wakefield accelerators, which use the inherently high current electron beams from laser wakefield acceleration (LWFA) as drivers for PWFA,[41] are also increasingly successful,[42–45] and will vastly expand capacities for PWFA and plasma photocathode-based electron beam production in the future. This means that there is a path for any laboratory that engages in state-of-the-art LWFA to realize inherently synchronized plasma photocathodes.[22]

The experimental and conceptual progress of plasma photocathode PWFA is accompanied by advancements in the theoretical description of particle-beam driven wakefields. The early models describing particle-beam driven wakefields considered only linear fluid theory or were restricted to non-linear theory in one spatial dimension.[17] Further, many were only applicable for a homogeneous plasma background. However, in the desirable blowout regime, non-linear theory is required for a proper description of the cavity. Later work such as refs. [46–48] gave more generalized approaches in this regime. Starting from the current densities in the quasi-static approximation, the radial equation of motion of an electron moving along the border of the blowout, $r = r_b(\zeta)$, can be calculated. The ordinary differential equation describing the blowout border is

$$A(r_b)r_b'' + B(r_b)(r_b')^2 + C(r_b) = \frac{\Lambda(\zeta)}{r_b} \qquad (1)$$

where $A(r_b)$, $B(r_b)$, $C(r_b)$ are the coefficient functions that depend on the (integral) ion density and the electron sheath of the cavity.[48] The function $\Lambda(\zeta)$ incorporates the presence of the driving and witness beam in terms of their respective current densities. Solving differential Equation (1) then yields the blowout radius $R_b(\zeta)$ as function of ζ for an arbitrary plasma channel density profile (as long as the density only changes radially). From the solution of the model the electromagnetic fields inside the blowout can be calculated. **Figure 5** shows that the solution of the

model is in good agreement with PIC-codes such as VLPL.[49,50] Assuming a constant ion density, the equations derived in ref. [46] can be recovered from this model, and further simplification yields the fields of phenomenological models such as.[51]

While these semi-analytical models generally yield good fits with PIC simulations, they are restricted to certain parameter regimes such that the assumptions made therein hold. A mutual disadvantage of all the aforementioned analytical theories is that the initial conditions for solving the ODE require external parameters, for example, from PIC simulations. One specific effect that is not well incorporated into the basic theory is the description of the divergence of the accelerating field in the blowout back. As a fix, both phenomenological functions for incorporating the divergence[52] as well as more complicated multi-sheath models[53] have been employed. On the basis of these models, electron injection and trapping can be considered. In ref. [54], trapping conditions for external injection of electron beams at varying angles and energies were derived, and as a simplified subset, can also be applied to cold Trojan Horse injection.

A first self-consistent theory presented in ref. [55] allows one to obtain the blowout radius simply from driver parameters and energy conservation laws. While this model is only applicable in the case of large blowouts, where the approximation $k_p r_b \gg 1$ holds, this is a desirable scenario for Trojan Horse injection to improve spatiotemporal injection precision and injected beam quality.

3. E-210: Trojan Horse at FACET

The "E-210: Trojan Horse" experiment was realized at SLAC FACET in 90° geometry between plasma wave and injector laser. This choice of geometry was a balanced outcome of experimental boundary conditions, and the strategy that enabled this first proof-of-concept realization. It involved the innovation, development and exploitation of the plasma afterglow diagnostics[56] and the so-called plasma torch downramp injection method[57,58] as stepping stones.

3.1. Experimental Setup

The FACET experiments took place in Sector 20 of the SLAC linac. Here, the high-current electron beam, generated by a thermionic cathode, compressed by a magnetic chicane and focused by a final focussing quadrupole system, interacted with a preionized plasma, as shown in **Figure 6**. The core experimen-
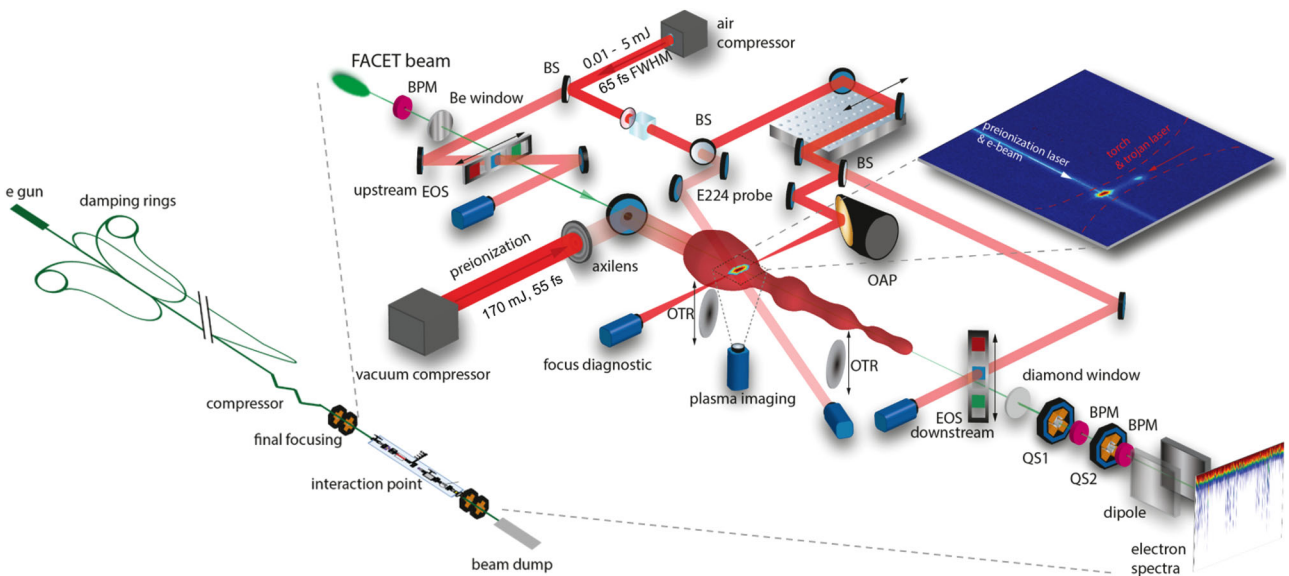
Figure 6. Setup of the "E-210: Trojan Horse" experiment at SLAC FACET. Key building blocks are FACET's electron driver beam, propagating through Beam Position Monitors (BPMs) and quadrupole systems (QS1 and QS2), the preionization laser pulse that generates a hydrogen plasma channel around the electron beam axis, Optical Transition Radiation (OTR) diagnostic screens, and auxiliary laser pulses derived from an air compressor. Beam splitters (BS) are used to send two pulses to Electro-Optical Sampling units, one is used to probe the plasma (E224 probe), and one, focused by an Off-Axis Parabolic (OAP) mirror is used as perpendicular injector laser pulse that ionized helium locally on electron beam propagation axis, thus enabling plasma afterglow, plasma torch and Trojan Horse experiments.
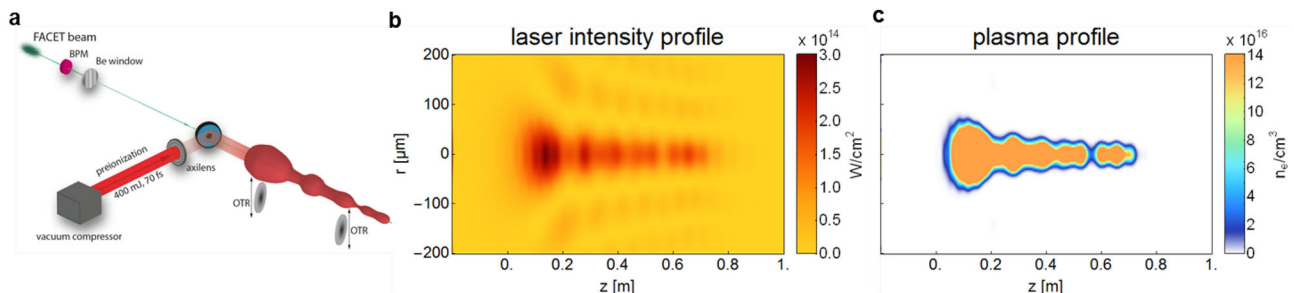

Figure 7. Relevant E-210 setup building block which produced the preionized plasma channel a); radial projection of the approximate intensity profile of the preionization laser while propagating in z-direction b); and corresponding hydrogen plasma profile produced by this intensity profile via tunneling ionization c).

tal setup was assembled in the picnic basket interaction chamber, which was designed collaboratively by Radiabeam Technologies for the "Plasma Photocathode Beam Brightness Transformer for Laser-Plasma Accelerators" project[59] to host the E-210 experiment, and to assist many others. The whole region between FACET's upstream beryllium window and downstream diamond window was filled with a 50:50 mixture of hydrogen and helium gas. A preionized plasma channel with plasma electron density of $n_e \approx 1.4 \times 10^{17}$ cm^{-3} was generated from hydrogen by a high-power laser pulse, focused by an axilens to moderate intensities. The laser pulse was then folded on the electron beam propagation axis by a holed mirror and exhibited an axial intensity profile such that its corresponding electric field exceeded the hydrogen tunneling ionization threshold around the propagation axis. As indicated in Figure 6, the resulting hydrogen plasma profile had a non-uniform width along the electron driver beam propagation axis.

Figure 7 concentrates on the relevant plasma preionization building block optics (Figure 7a), provides a representation of the projected (calculated) laser intensity profile produced from the axilens (Figure 7b) and shows the resulting (calculated) hydrogen plasma profile in projection (Figure 7c). An important feature of laser-based preionization methods is that once the threshold of full ionization is reached and locally 100% of the gas is ionized, shot-to-shot local intensity jitter does not matter as long as the full ionization intensity threshold is exceeded. This inherent levelling feature due to the intensity threshold is clear from comparing Figure 7b,c). This new type of plasma source with new capabilities complements other sources used elsewhere in PWFA and in LWFA. The selective ionization of hydrogen, without ionizing helium in the mix, in a large volume, was an enabling success achieved within E-210. However, the extent of the volume where the threshold of full ionization is reached, is critical. Very consequentially, the width of the channel obtained in the experiments

**ADVANCED
SCIENCE NEWS**

www.advancedsciencenews.com

*annalen
der* **physik**

www.ann-phys.org

was limited to approximately 100 μm. For the most time during propagation of the plasma wave through the channel over its maximum length of $\Delta z \approx 65$ cm, the channel radius r_c was significantly narrower than the nominal blowout radius R_b. This non-uniformity was a bottleneck and limitation in the experiment.

Timing of the preionization laser with respect to the electron beam arrival could be tuned. The laser-generated plasma is comparatively cold and long-lasting due to the comparatively low intensity of the laser pulse. Hence, hydrodynamic effects impact plasma channel shape and density significantly only over extended timescales, toward the ns-range. Plasma heating effects are an important field of study with regard, for example, to high repetition rate challenges of plasma-based accelerators.[42,60,61] However, systematic studies of plasma heating effects were outside the core scope of E-210. Here, we were content with the preionization laser arriving $\simeq 20$ ps before the electron beam, which ensured steady operation, unaffected by shot-to-shot preionization timing jitter.

In contrast, the timing of a second laser pulse which was strongly focused perpendicular to the electron beam path, was important on the fs-ps timescale. This laser pulse was crucial both for diagnostics as well as for injection of electrons to produce witness beams in the plasma wave. Hence, we installed Electro-Optical Sampling (EOS) units upstream and downstream of the main plasma interaction, based on further split-off laser pulses. The EOS provided time-stamping of shots, and benchmarking for the newly developed concept of plasma afterglow metrology.[56] The energy, transverse pointing, and delay of the plasma photocathode injector laser pulse could be varied, such that the laser pulse would ionize varying amounts of helium in a local filament across the electron driver beam axis. The laser energy budget was up to 5.3 mJ, the transverse tuning range with respect to the electron driver beam axis covered a few hundred μm, and the temporal tuning range covered a range of few ps around the electron beam arrival time.

3.2. Preionized Plasma Channel Limitations

This narrowing plasma channel shape has profound impact on the effective blowout shape, and hence on the corresponding evolving electrostatic potential and electric field profile of the wake. This effect of partial or not wide enough preionization has been discussed, for example, in ref. [62], and the need for the wakefield to fit into the plasma channel width has been highlighted and investigated in ref. [21]. At FACET in E-210, this meant that several regimes of PWFA were realized along the plasma channel during one and the same shot. This plasma channel-induced blowout deformation and the behavior of the plasma wave as it undergoes propagation in an increasingly narrower plasma channel is exemplified in **Figure 8**, which shows the plasma electron charge density, based on 3D PIC simulations with VSim[63]

In Figure 8a, the cylindrical plasma channel radius $r_c = 60$ μm, and the expelled plasma blowout electrons see a re-attractive hydrogen ion background everywhere on their trajectories as they form the blowout shape, even at the point of maximal displacement from the axis, which is determined by the plasma density

and the driver beam (shown in black) current profile I (red solid line, shown at the bottom of the figure as projection of the longitudinal current profile of the Gaussian electron beam). The longitudinal electric field profile E_{acc} on axis is shown as a dark red plot, and the underlying corresponding electrostatic trapping potential $\Delta\Psi$ is shown in blue. This situation represents the textbook case of a fully non-linear plasma wake in the blowout regime.

When the plasma channel narrows to $r_c = 45$ μm as shown in Figure 8b, it is still just as wide as the nominal blowout radius R_b, and hence the blowout shape in the first bucket and its electric field profile is in first approximation similar as in the case shown in Figure 8a. However, plasma channel edge effects begin to impact the blowout structure. Some of the plasma electrons leave the ion channel and see a reduced re-attractive plasma potential. This results in plasma frequency redshifting and an elongated plasma wave. In particular, the second (and third) buckets are impacted substantially by the narrow plasma channel.

When further narrowing the plasma channel radius to $r_c = 30$ μm, the restoring force of the ions is reduced significantly for electrons around their turning point as they reach a region where the ion density decreases sharply in the transverse direction. Here, a qualitative threshold is exceeded and the blowout breaks down, forming a much weaker plasma wave, as displayed in Figure 8c. The constraints of the plasma channel width are reflected by the onset of 'snow-ploughed' plasma electrons,[64] which do not return to axis on the time scale of $1/\omega_p$ but are simply expelled outward by the electron driver beam.

When the channel radius is trimmed to $r_c = 15$ μm in the simulation, most plasma electrons are snow-ploughed away, and the driver beam leaves behind an evacuated ion channel with constant and uniform density. Practically no plasma blowout structure remains despite a decelerating field at the driver beam position: the longitudinal electric field is approximately zero behind the driver beam, while the ion channel still exhibits linear focusing forces. This, in effect, represents a *wakeless regime*, in which the electron driver beam expels plasma electrons to leave behind a pure focusing ion channel as shown in Figure 8d).

We emphasize that these highly complex channel-induced plasma wake dynamics, plasma blowout lengthening and the wakeless regime in the pure ion channel presented in Figure 3 are not theoretical scenarios but indeed have been encountered during the realization of E-210. This is the logical consequence of the different plasma channel widths experienced by the plasma wake during propagation through the channel. In fact, the scenarios described above have very likely been repeatedly realized during each shot, as a result of the plasma channel radius decreasing and increasing repeatedly in the range from 0 to ≈ 100 μm.

As described in ref. [21], the limited channel width did impose a minimum hydrogen plasma density to be used, which forced to operate with a smaller-than-optimal blowout size, and in turn put stricter demands on spatiotemporal alignment and synchronization for plasma photocathode injection. This working point was in fact close to a ceiling of employable plasma densities, that arises from unwanted ionization by the wake and the electron driver beam fields.[62] In Section 3, we will reiterate the supplementary discussion in ref. [21] on how a wider plasma channel and operation at lower plasma densities can stabilize the PWFA and plasma photocathode combination substantially.
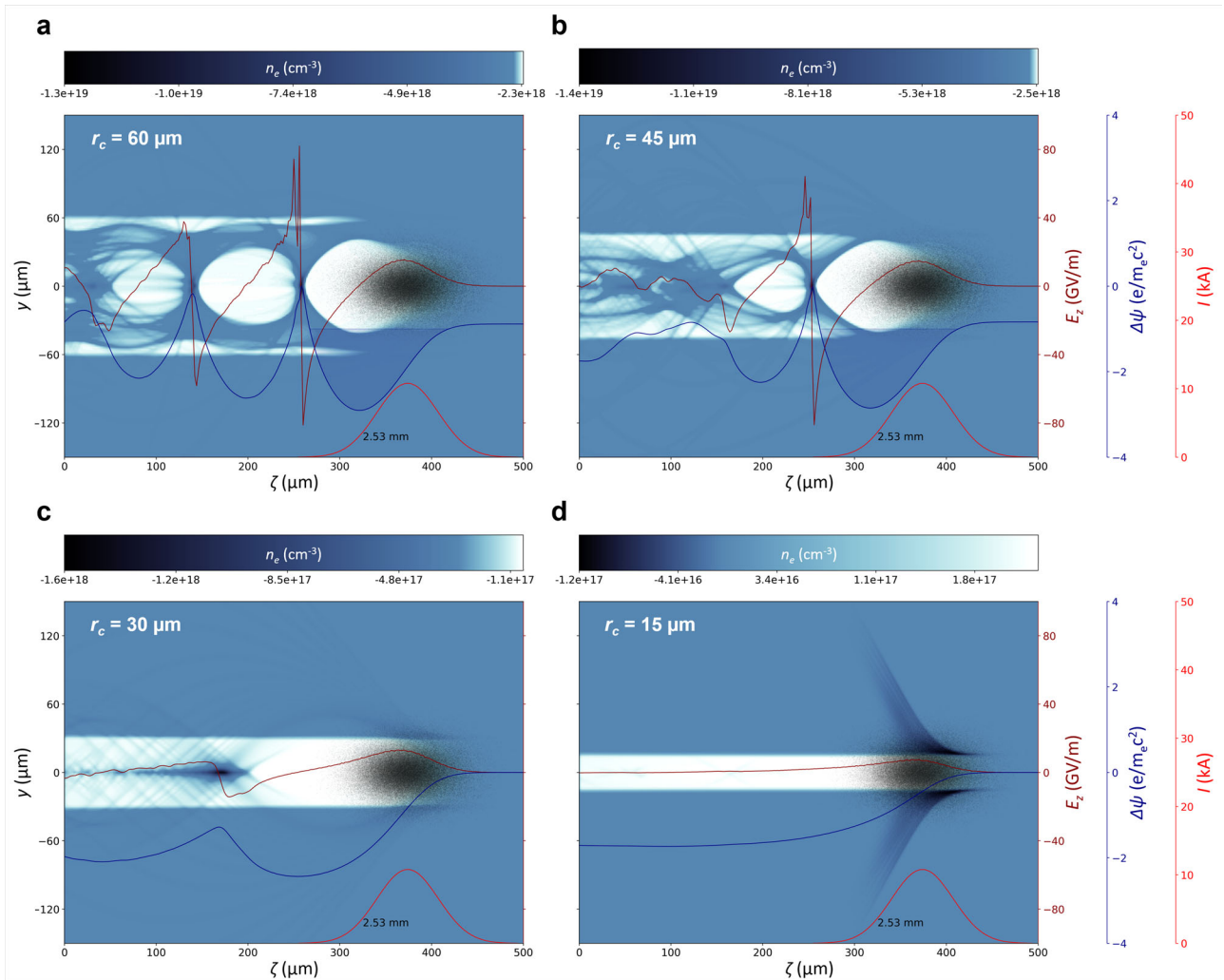
Figure 8. 3D PIC-simulations (VSim) of intense electron beam interaction with a preionized plasma channel of different radii r_c. The FACET electron driver beam (black) propagates to the right, expels plasma electrons and sets up a nonlinear PWFA blowout as in (a,b), or for a thinner channel generates a wakeless ion channel as in (c,d) that could be used, for example, for light source applications.

3.3. Energy Gain Limitations

In addition to the maximum channel width bottleneck and the need to squeeze the plasma wave through it, the quasi-periodically narrowing and expanding plasma channel had a profound effect on the energy gain of injected electrons in the plasma wakefields.

The unfavorable topology after the injection point at $z \approx 20$ cm (dashed red line in **Figure 9**a) impacted the blowout shape and size along the propagation distance, resulting in a substantial variation of the effective wakefield phase at the witness beam trapping position.

Simulations show that the witness beam actually underwent a quasi-periodic transition from accelerating to decelerating phase of the wakefield. In ref. [21] (Figure S2 therein) we estimated projected energy gain outcomes for realistic trapping positions considering this wakefield evolution over the full plasma interaction distance of $\Delta z \approx 65$ cm, while in the present work Figure 9a shows a waterfall plot of the corresponding on-axis accelerat-

ing electric field evolution during propagation along the plasma channel. The figure highlights the shortcomings of the varying plasma channel and its significant effect on the longitudinal wakefield. Further, it explains the effective energy gain limitation encountered in the E-210 experiment.

Experimental boundary conditions were responsible for restriction of the injection position at $z \approx 20$ cm. Numerical simulations indicate that, for example, an injection position at around $z \approx 10$ cm, where the plasma channel reaches maximum width, would have allowed harnessing the full accelerating field of 50–60 GV m^{-1} over an extended distance. Estimates of this scenario show potential witness beam energy gains of multi-GeVs, instead of ≈ 1 GeV as in our proof-of-concept experiments.[21] This is supported by simulations of driver beam interaction with the preionized plasma and its deceleration to an average energy of $\Delta W_{\text{sim}} \approx 5.4$ GeV FWHM shown in Figure 9b. The simulation data represents the strongest deceleration scenario for a shot with optimal alignment and maximum plasma channel size. Corresponding measurements of the driver beam deceleration
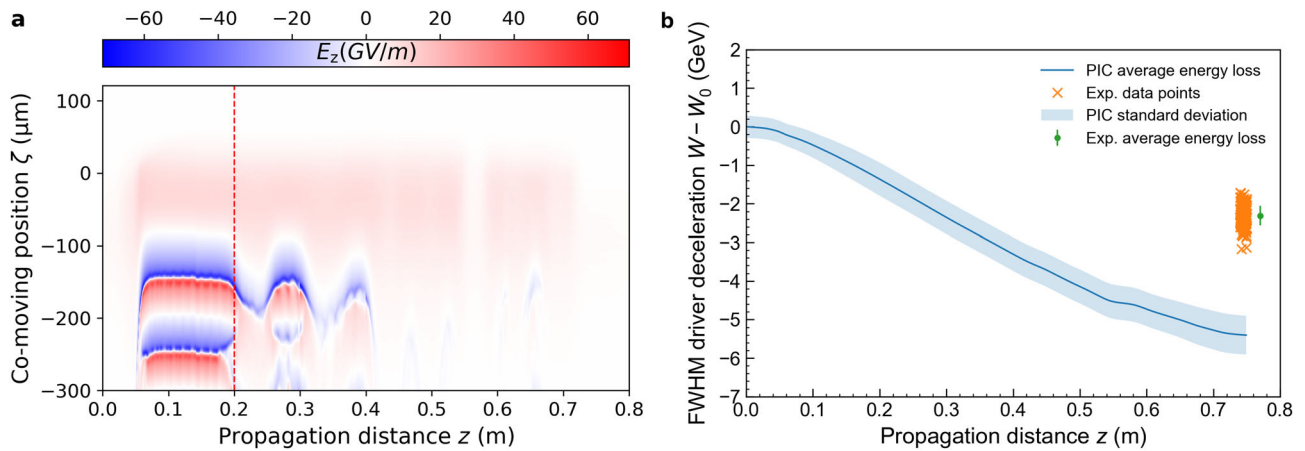
Figure 9. a) shows the on-axis longitudinal wakefield evolution of blowout when propagating through preionized plasma channel shown in Figure 7c, and b) shows estimates of driver beam deceleration obtained from PIC simulation and measured at the experiment. In (a), the vertical red dashed line denotes the experimental injection position of the witness beam. In (b), the blue solid line shows simulated driver beam deceleration of $\Delta W_{sim} \approx 5.4$ GeV FWHM. The transparent tubes represent the standard deviation interval. The orange crosses represent measured data points of FWHM driver beam deceleration and the green point shows the average over 200 consecutive shots at $\Delta W_{exp} \approx 2.3$ GeV with corresponding standard deviation error bars.
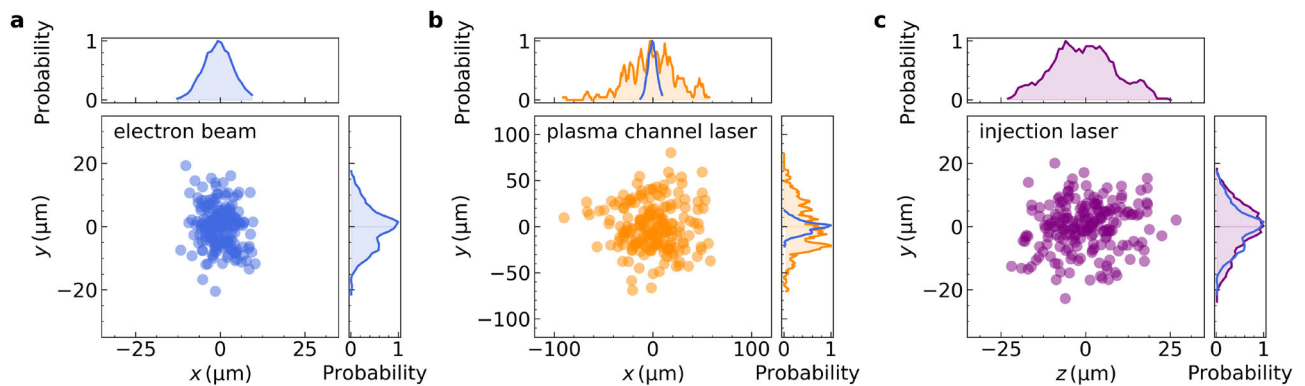

Figure 10. Typical pointing jitters on target of electron driver beam a), preionization plasma channel laser b) and plasma photocathode injection laser c) encountered during the E-210: Trojan Horse experiment at FACET. In subset plots, the sold lines show the jitter distributions in the corresponding plane normalized to the maximum value. In (b,c) subset plots, additionally, electron driver beam jitter distributions (solid blue line) are presented for direct comparison.

(orange crosses) are consistent with the simulation but show a somewhat reduced average driver beam deceleration of FWHM $\Delta W_{exp} \approx 2.3$ GeV in a range from $\Delta W_{min,max} \approx 1.7$–3.1 GeV. Reduced driver beam deceleration can be attributed to sub-optimal alignment and/or plasma channel size, and the large variation of experimentally observed driver beam deceleration is further evidence of strong shot-to-shot fluctuations.

While wakefield dynamics induced by the plasma channel topology were a limiting factor during the experimental campaign, they are an interesting subject in their own right. For example, the wakeless regime can be an attractive operation point for betatron radiation generation and ion-channel lasers.[65,66]

3.4. Injection Considerations and Procedure

At the core, the injection stability is a function of plasma blowout size on the one hand, and spatiotemporal alignment and synchronization precision with respect to the plasma photocathode injection laser on the other hand. Increasing the plasma blowout size by operating at reduced plasma densities therefore would increase the relative injection precision for a given absolute shot-to-shot jitter, for example, with regard to the pointing of the injector laser. However, in case of E-210, a larger blowout would also have meant that any shot-to-shot jitter of the preionization laser with respect to the driver electron beam axis would have brought the blowout closer to the boundaries of the plasma channel or even would mean partial, asymmetric destruction of the blowout when it touches the plasma channel boundaries. **Figure 10** summarizes typical experimentally encountered shot-to-shot spatial jitter of the electron driver beam (Figure 10a), the preionization plasma channel laser (Figure 10b), and the injection laser (Figure 10c): the experimental shot-to-shot spatial jitter of the plasma channel preionization laser was substantially larger than that of the electron beam, or the injection laser. This constellation further emphasizes the large impact of the preionization laser configuration on the E-210 experiment injection studies.
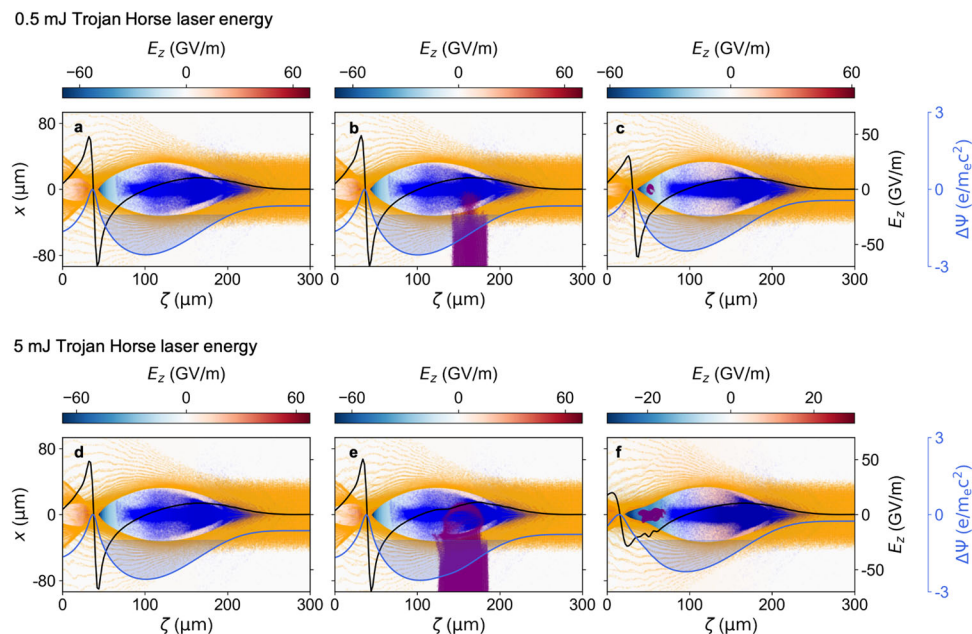
Figure 11. Snapshots from PIC-simulations with VSim for the E-210 scenario. The top panel shows the situation before a) at $t = 0$, during b) at $t \approx 667$ fs and after c) injection at $t \approx 9.3$ ps with an injector laser pulse at 0.5 mJ; the bottom panel shows the corresponding situations when using 5 mJ injection laser energy.

Despite those jitters, using the spatiotemporal afterglow response[56] and the plasma torch injection mechanism[57,58] enabled finding the suitable pointing and timing of the injector laser with respect to the plasma wave at the interaction point, and thus to access the plasma photocathode injection regime. **Figure 11** visualizes 3D PIC simulations of the E-210 experiment. The electron beam driver (blue) propagates to the right, and drives a blowout that only just fits into the hydrogen plasma channel (orange dots) at the injection position $z \approx 20$ cm. The top panel shows the situation for the injector laser pulse energy of 0.5 mJ, while the bottom panel represents the 5 mJ case. The plasma photocathode injector laser pulse (not shown directly) with pulse duration of 65 fs (FWHM), and vacuum spot size of $w_0 = 20 \mu m$ (r.m.s.) is propagating from bottom to top, ionizes helium, and thereby releases initially "ultra-cold" helium electrons (purple) inside, but also outside of the wake due to its rather long Rayleigh length $Z_R = \pi w_0^2 / 0.8 \mu m \approx 1.57$ mm compared to the blowout diameter of few tens of μm. The solid black and blue profiles highlight on-axis longitudinal wakefield E_z and trapping potential $\Delta\Psi$, respectively. When the plasma wakefield swipes through, only those helium electrons that are released within the electrostatic potential region of the wake that is capable of trapping electrons from rest (indicated by the blue transparent region) are captured by the plasma wave, while the other laser-released helium electrons are lost to the background plasma. Frame (a,d) represents the situation before the laser pulse enters, and frames b) and e) show the He electrons (purple) appearing as a result of the plasma photocathode laser pulse ionizing helium. Frame (c,f) then present the formed and trapped witness electron bunch with low charge (c) and high charge (f) as a result of the different injector laser energies. The higher injected charge for the 5 mJ case is a result of the large ionization volume inside the blowout. This can be seen by comparing the ionization tracks in

Figure 11b,e, showing that for the 5 mJ case the ionization track is substantially wider compared to the 0.5 mJ laser energy case.

The realization of the first proof-of-concept demonstration of the plasma photocathode, and the many other scientific firsts realized during E-210, represent experimental milestones toward production of ultracold electron beams. However, so far only the tip of the iceberg has been revealed. To reach the full potential of the plasma photocathode, several aspects are important to recognize. First, in E-210, the large ionization volume of the injection laser pulse even in the 0.5 mJ case, with a comparatively long Rayleigh length, fills a large fraction of the comparatively small plasma blowout, which ultimately results in a large initial phase space volume and increases the obtainable emittance of the trapped witness beam. Second, because of the rather long driver beam compared to the blowout size, helium electrons are released in its immediate space charge field. They, therefore, are kicked out transversely by the driver beam to some extent and thereby obtain significant transverse momentum, which likewise increases the emittance. In the E-210 scenario and its boundary conditions, the obtainable normalized emittance minimum, therefore, is at the single μm-rad scale for the plane in the laser propagation axis, and slightly better in the other transverse plane, since the electron release is not spread out across the entire extent of the blowout in this plane. This is predicted by simulations and is consistent with the experimentally derived emittance,[21] and thus shows that the plasma photocathode principle works exactly as anticipated. At the same time, it was shown that plasma photocathodes can be realized even under sub-optimal boundary conditions, which is encouraging for future, broader and improved implementations of the scheme. Given that the driver beam normalized emittance at FACET was of the order of 100 mm-mrad in both transverse planes, respectively, and the experimentally derived emittance of the witness beam was of the order

**ADVANCED
SCIENCE NEWS**

www.advancedsciencenews.com

*annalen
der* **physik**

www.ann-phys.org

µm-rad and the current likely of kA-scale, also the goal of a "Beam Brightness Transformer" as a partial result of the "Plasma Photocathode Beam Brightness Transformer for Laser-Plasma Accelerators" project[59] can be considered to be demonstrated in this proof-of-concept, with a 5D brightness transformer ratio of up to 100.

Summarizing, the FACET E-210 experiment was successful in demonstrating key milestones such as the feasibility of plasma photocathode injector,[21] realization of the first density-downramp injection in PWFA,[58] by demonstrating novel plasma-based diagnostics with large potential for non-interceptive precision metrology,[56] and by demonstration of the principle of the "Beam Brightness Transformer". The experimental results, lessons learned, and modeling and understanding, also are crucial to designing and preparing the next generation of experiments. Wider plasma channels for more stable injector and accelerator operation and larger energy gains, reduction of the ionization volume of the injection laser for full charge capture and lower emittances and/or different injection geometries, specifically collinear, are amongst the top priorities for future installations of plasma photocathodes at FACET-II and elsewhere. In the following, we summarize lessons learned and provide further insight into such advanced versions of plasma photocathodes, using FACET-II as showcase.

4. E-310: Trojan Horse-II at FACET-II

The E-310: Trojan Horse-II program at SLAC FACET-II aims at investigating various plasma photocathode configurations, for example the realization of collinear and near-collinear geometry, innovative approaches for reduced effective Rayleigh length of the plasma photocathode laser[30] and many other variations. A wider plasma channel with larger blowout sizes combined with improved incoming stability of driver electron beam and laser beams will help to make headway toward improved witness beam quality, tunability, and stability. Even in 90° geometry these improvements promise much better stability and output beam quality. The next sections will discuss some of these aspects.

4.1. Future Capabilities at FACET-II

The implementation of collinear geometry and/or confined laser release volumes and/or mitigation of driver beam kick to the released electrons, is suitable to allow production of witness beams with increasingly improved emittance and brightness, as pointed out in ref. [21]. Operation at reduced plasma densities, which requires wider preionization channels, can decrease the residual and correlated energy spread of the witness beam.[40] Further, reduced plasma density does also relax the demands on the driver beam charge density, since the blowout regime can then be achieved easier. A reduced driver beam density (and transverse matching) also elegantly avoids hot spots that may otherwise produce dark current, and the decreased plasma density naturally decreases potential wakefield vertex hot spots.[62]

We emphasize again that if the plasma channel can be made wide enough by a sufficient margin, shot-to-shot variations of pointing, energy and wavefronts of the preionization laser pulse

may not have any influence at all on the plasma blowout shape: even if jitter in these parameters leads to variation of the channel width from shot-to-shot, it would not impact the acceleration process, as long as full ionization saturation is realized in the overlap region with the plasma wave, and the channel fully encompasses the passing blowout structure, see Figure 8a,b.

When the accelerating and focusing electric field profile is hence constant, and the plasma blowout is larger and/or the electron driver beam is shorter than in E-210 so that there is no driver beam kick that could increase the transverse momentum of released HIT electrons, realization of witness bunches with normalized emittances increasingly approaching the nm rad level, and hence ultrahigh brightness can be achieved in E-310. This is consistent with earlier works and estimations of emittance and brightness in plasma photocathode scenarios.[22,23,27,29,30,32–35,38,40,67] **Figure 12** visualizes and contrasts the E-210 scenario (top panel) with a potential E-310 scenario (bottom panel). The electron driver beam (green) propagates from top left to bottom right and excites the plasma wave. The plasma photocathode laser pulse (red) releases He electrons, which then form the trapped witness bunch. Key differences of these scenarios are the injection geometry (perpendicular vs collinear) and the blowout size.

4.2. Beam Parameter Stability and Tuneablity

While generation and acceleration of high-quality electron beams is a supreme focus for plasma-based accelerator research, in addition, the reproducibility and tunability of the output beam parameters are crucial toward realization of key applications such as free-electron lasers and, prospectively, fundamental physics such as probing of quantum electrodynamics or high energy physics applications and perhaps linear colliders. The central importance of emittance and beam quality of electron beams for various applications is highlighted, for example, in US[68] and UK[69] roadmaps.

In conventional accelerators, a detailed statistical analysis is performed to identify prime sources of jitter, and subsequently, a systematic approach is taken to eliminate or to minimize these jitter sources at the origin.[70] Similar strategies are required for plasma-based accelerators. Here, witness beam output parameter variation from shot-to-shot can be attributed to two major sources: the jitter of the plasma *accelerator* on the one hand, and jitter of the witness beam *injector* process on the other. In the Trojan Horse approach, accelerator and injector are largely decoupled, in contrast to other plasma accelerator injection schemes, where the injection rate depends crucially on the wake excitation and gas or plasma density profile encountered in a specific shot.

With regard to the *acceleration*, variations of plasma source and the incoming electron driver beam determine the size, strength and evolution of the plasma wakefield accelerator. As described in Section 2, the main sources of jitter in the E-210 experiment originated from shot-to-shot variations of the preionization laser pulse as shown in Figure 10b, and periodic narrowing of the plasma channel as presented in Figure 7. This accelerator building block can be substantially improved and impact of preionization laser jitter may even be fully eliminated as discussed earlier. Driver beam parameter stability can be significantly improved, at
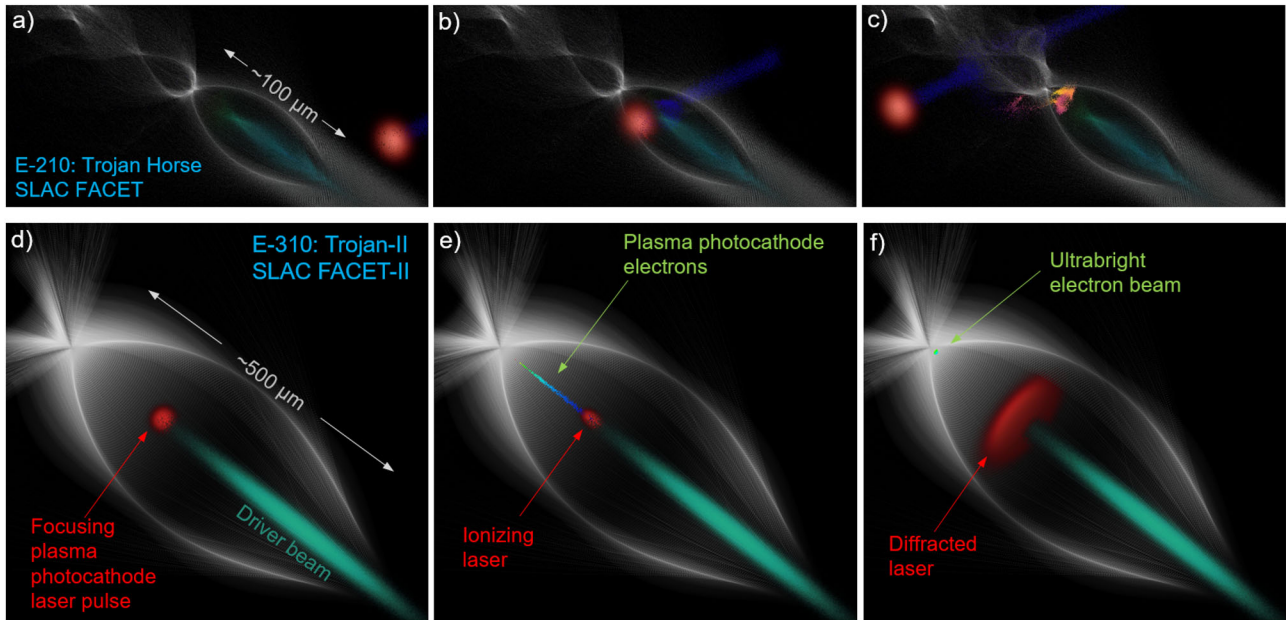
**ADVANCED
SCIENCE NEWS**

www.advancedsciencenews.com

annalen
der **physik**

www.ann-phys.org

Figure 12. The top panel shows a 3D visualization of the E-210 scenario before (a), during (b), and after (c) He electron release in a comparably small blowout. The bottom panel shows the corresponding situation for E-310 in collinear and co-propagating geometry.

FACET-II, for example, by beam generation from a state-of-the-art photocathode.

With regard to the witness beam *injection*, primary factors that affect the plasma photocathode process are spatiotemporal alignment and synchronization of the injection laser with respect to the plasma wakefield accelerator, and the laser pulse intensity. Fortunately, the plasma photocathode injection method offers control and stabilization advantages resulting from the inherently decoupled nature of this method. The robustness of the scheme when encountering even significant spatiotemporal jitter of the injector laser was regarded and shown via simulations already in the original publication.[22] Impact of laser intensity variation was likewise studied and shown, for example, in ref. [27, 33, 71] for collinear, co-propagating plasma photocathode injection laser in ref. [34] for a variation of the plasma photocathode scheme. Here, we provide further insight into how these previously identified main plasma photocathode injector jitter sources i) temporal jitter, ii) transverse spatial jitter, and iii) intensity jitter of the plasma photocathode injector laser pulse impact the witness beam stability, using 3D PIC-simulations. Similar parameter studies have previously been conducted and presented to the community and similarly have been used to establish confidence in the possibility of stable operation of X-ray free-electron lasers with plasam photocathode-generated electron beams.[72]

The simulation parameter space regarded here is informed by the results and discussions from Sections 3 and 4. The electron driver beam reflects a possible working point within the FACET-II parameter space range, such that its energy is set to $W = 10$ GeV and its charge to $Q_d = 1.5$ nC. The hydrogen plasma and helium gas density are set to $n_p \approx 1.78 \times 10^{16}$ cm^{-3} and $n_{He} \approx 2.27 \times 10^{17}$ cm^{-3}, respectively. The hydrogen plasma density corresponds to a plasma wavelength $\lambda_p \approx 250$ μm, and the driver beam produces an elliptical blowout of similar length

$L_b \approx 250$ μm and radius of $R_b \approx 65$ μm. The transverse normalized emittance of the driver beam is matched to the hydrogen plasma density n_p, using $\sigma_{x,y} = \sqrt{\epsilon_n/\gamma k_\beta}$, where ϵ_n is the driver beam normalized emittance, $k_\beta = \omega_p/c\sqrt{2\gamma}$ is the betatron wavenumber, ω_p is the plasma frequency, c is the speed of light and γ is the relativistic Lorentz factor of the FACET-II electron driver beam. The longitudinal size of the driver beam is optimized according to $\sigma_z = \sqrt{2}/k_p$ to satisfy the PWFA resonance condition, where $k_p = \omega_p/c$ is the plasma wavenumber. The normalized emittance $\epsilon_{n,x,y} = 50$ mm mrad of the drive beam determines $\sigma_{(x,y),rms} \approx 4.5$ μm and the resonance condition yields $\sigma_{z,rms} \approx 56$ μm, however, we reduced the driver beam length to $\sigma_{z,rms} \approx 32$ μm to avoid overlap with the injector laser release position.

Figure 13 visualizes the underlying scenario. The electron driver beam (black) propagates to the right and sets up the plasma blowout in its wake. The plasma photocathode laser pulse is currently in the process of releasing He electrons (purple) via tunneling ionization of the background He gas, with some of those electrons that have been released at the beginning of the injection process at $\zeta_i = z - ct \approx 161$ μm already piling up at the trapping position ζ_f within the blowout, which is defined by the electrostatic potential $\phi(\zeta) \propto \int E_z(\zeta)d\zeta$ at each of the release slices. The corresponding on-axis electrostatic trapping potential $\Delta\Psi = \Psi(\zeta_i) - \Psi(\zeta_f) = -m_e c^2 e^{-1}$ of the wake, with $\Psi(\zeta) = em_e^{-1}c^{-2}\phi(\zeta)$, is shown in blue, and the region in which plasma photocathode-released electrons would be trapped, corresponding to $\Delta\Psi \leq -1$, is represented by the blue shaded area, just as previously in Figure 11. The default release position ζ_i of He electrons is in the center of the hydrogen-based blowout, where the corresponding trapping potential has its minimum $\Delta\Psi_{min} \approx -1.7$. The He electrons are born at rest, and hence are slipping backward toward

**ADVANCED
SCIENCE NEWS**

www.advancedsciencenews.com
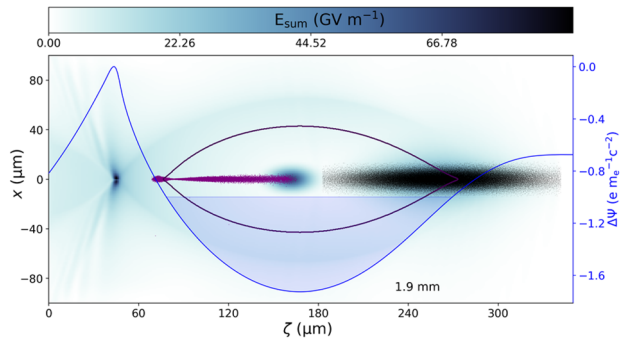
annalen
der **physik**

www.ann-phys.org

Figure 13. Visualization of the plasma wakefield scenario used for the plasma photocathode parameter sensitivity studies. The driver beam (black) propagates to the right and the plasma photocathode laser pulse releases He electrons (purple) in the centre of the blowout. The purple ellipse indicates the extent of the region where electrons released would be trapped.

the blowout vertex while being quickly accelerated to relativistic energies due to the multi-GV m^{-1} accelerating gradient. The purple solid ellipse approximates the trapping volume, that is, electrons released approximately within this volume from rest will be trapped by the electrostatic potential of the wave. The sum of the combined electric field is plotted, thereby showing the focused plasma photocathode laser pulse in the center of the blowout. The collinear plasma photocathode laser pulse has a FWHM pulse duration $\tau = 50$ fs, an r.m.s spot size $w_0 = 7$ μm and a default focus intensity in terms of the dimensionless laser amplitude $a_0 = 0.018$ (the same parameters as used for Figure 2a). We note that plasma photocathode injector parameters are purposefully optimized for a low witness charge regime to minimize space charge and beam-loading effects, in order to focus on the impact of incoming injector laser pulse jitter contributions. Much higher witness charge values are possible to be released, for example straightforwardly by increasing the laser pulse intensity, or by increasing the He density. At elevated witness charge and current levels, advantageous effects of beam-loading can be harnessed, while at even higher charge and current levels, the beam and its emittance become space charge-dominated.

Importantly, because of the parabolic shape of the trapping potential, its slope around the potential minimum is shallow. Therefore, the deviation in initial $\Delta\Psi(\zeta_i)$ around the release position is small, and consequently, even when electrons are released across an extended co-moving range by the laser pulse, this provides a strongly reduced spread in final trapping position $\delta\zeta_f$, and thus enables fs to sub-fs duration of the formed bunches without additional measures. This does not only constitute an automatic bunch compression of the injected electrons but furthermore releasing electrons at this prominent position in the centre of the blowout makes it intrinsically resilient against relative timing variation. Even when electrons are released at different longitudinal co-moving positions around the default release position from shot-to-shot, they are trapped at similar accelerating phase positions in the wake. Because of the phase-locked feature in beam-driven acceleration, this manifests itself in significantly reduced witness beam energy variation from shot-to-shot. This robustness toward spatiotemporal release jitter was first seen in ref. [22] (also see supplemental material therein).

Following a similar derivation as in refs. [73–75], the final trapping position can be expressed as a function of initial release position and plasma density as

$$\zeta_f = -\left(\zeta_i^2 + \frac{4\alpha_t}{n_p}\right)^{1/2} \qquad (2)$$

where $\alpha_t = m_e c^2 \epsilon_0 e^{-2}$ and ζ_i is the initial release position within the trapping potential. Note that in this representation the potential minimum is at $\zeta_i = 0$. Series expansion of Equation (2) at $\zeta_i = 0$ yields $\zeta_{f,t} \approx -2\sqrt{\alpha_t/n_p} - \zeta_i^2/4\sqrt{\alpha_t/n_p} + \mathcal{O}(\zeta_i^4)$. From this we can immediately see that due to the quadratic ζ_i term, releasing electrons at the trapping potential minimum, meaning $\zeta_i \approx 0$ here, is an optimum that results in maximized stability of the trapping position ζ_f. Further, we can see again that lower plasma densities improve injection stability.

Based on this general injection setup, simulations can be performed to quantify the impact of jitters for more specific cases. For example, experimentally measured, setup-specific values of jitters can be taken into account if known, for example, the experimental spatiotemporal jitter of the plasma photocathode laser encountered in E-210 (compare Figure 10), or project-specific target values for expected spatiotemporal and laser intensity jitters can be assumed. The next section gives insight into the impact of jitters of the spatiotemporal release position and laser intensity around a target working point at FACET-II based on above settings.

4.3. Injector Laser Timing Jitter

First, the longitudinal release position was varied by shifting the plasma photocathode laser longitudinally in the range of $\Delta\tau = 30$ fs, while keeping all other settings constant at the above-discussed default parameters. Stability toward longitudinal release position jitter variation was first shown in ref. [22]. The choice of this range is informed by the typical level of synchronization that can be achieved in state-of-the-art linacs, for example, used for X-FEL machines. **Figure 14** shows the 3D PIC simulation results obtained by VSim over a propagation distance of 0.8 cm. In order to capture the large blowout structure in its entirety and at the same time resolve relevant physics of PWFA, the co-moving simulation box consists of $N_z \times N_x \times N_y = 358 \times 217 \times 217 \approx 16.8$ million cells with a spatial resolution of 1 μm in each direction and an integration time step of $\Delta t \approx 2$ fs. The background hydrogen plasma is modeled with one macro-particle per cell (PPC). Absorption boundary layers are utilized to minimize field reflections. The neutral helium is implemented as a fluid gas with a PPC of 1000, which increases the number of macro-particles in the witness beam and improves simulation fidelity. The solid lines represent the average value over all simulations performed in 5 fs-steps up to the maximum delay of ± 30 fs. The shading shows the standard deviation interval around the baseline.

From top to bottom, the evolution of energy gain W (left y-axis), relative energy spread $\Delta W/W$ (right y-axis), the resulting witness bunch length $\sigma_{z,rms}$ (left y-axis), peak current I_{peak} (right y-axis), normalized emittance $\epsilon_{n,x}$ in x-direction and the other
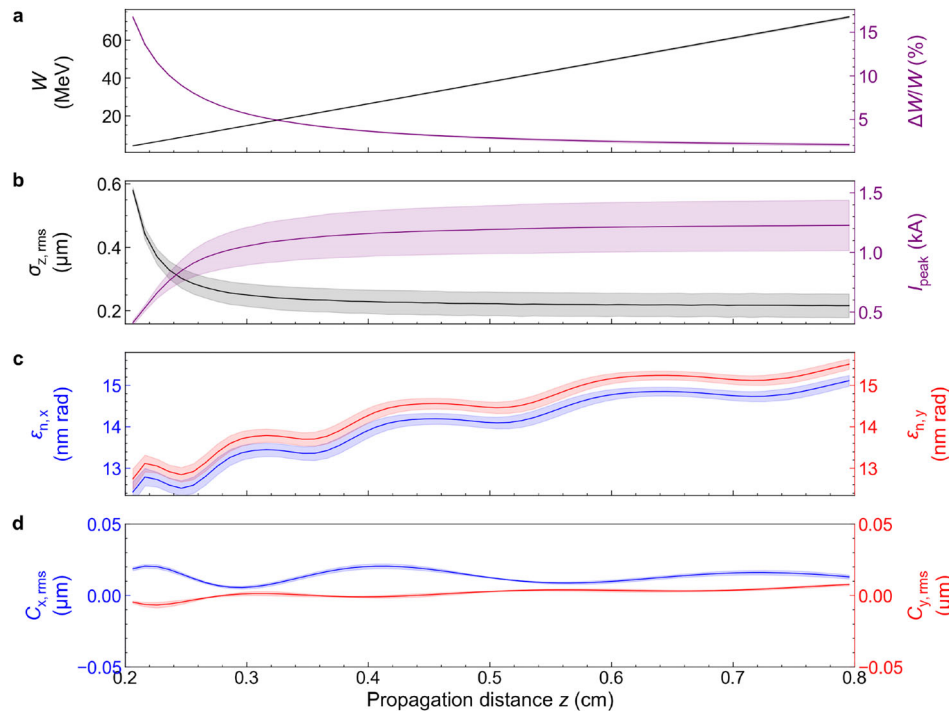
Figure 14. Evolution of witness bunch parameters versus temporal jitter of 30 fs of collinear plasma photocathode laser pulse release position. From top to bottom, the evolution of energy gain W (left y-axis), relative energy spread $\Delta W/W$ (right y-axis), the resulting witness bunch length $\sigma_{z,rms}$ (left y-axis), peak current I_{peak} (right y-axis), normalized emittance $\epsilon_{n,x}$ in x-direction and the other transverse plane $\epsilon_{n,y}$, and witness beam centroid $C_{x,y,rms}$ in both planes are plotted as a function of propagation distance z.

Table 1. Witness beam parameter summary of plasma photocathode laser jitter analysis.

Beam parameter	Timing jitter $\Delta\tau$	Pointing jitter ΔX	Laser amplitude jitter Δa_0
Energy W (MeV)	72.38 ± 0.69	72.15 ± 0.59	71.69 ± 0.68
Energy spread (%)	1.52 ± 0.11	1.41 ± 0.05	1.38 ± 0.15
Charge (pC)	2.375 ± 0.006	2.371 ± 0.005	2.41 ± 0.42
Peak current I_p (kA)	1.23 ± 0.21	1.32 ± 0.21	1.56 ± 0.11
Bunch length (µm)	0.22 ± 0.04	0.19 ± 0.03	0.17 ± 0.02
Normalized emittance $\epsilon_{n,x}$ (nm rad)	15.11 ± 0.13	29.91 ± 11.80	15.17 ± 1.77
Normalized mittance $\epsilon_{n,y}$ (nm rad)	15.51 ± 0.12	15.38 ± 0.48	15.66 ± 1.90
5D brightness ($\times 10^{18}$ A m^{-2}rad^{-2})	10.45 ± 1.65	7.11 ± 3.66	13.5 ± 2.40

transverse plane $\epsilon_{n,y}$, and witness beam centroid $C_{x,y,rms}$ in both planes are plotted as a function of propagation distance.

The witness beam energy, energy spread, normalized emittance, centroids, and charge are particularly unaffected by temporal injection laser shifts (also see summary **Table 1**), as expected from previous simulation scans such as.[27] The bunch duration and peak current are slightly more impacted by the timing jitter. As discussed previously, the excellent output beam parameter stability arises from the fact that the trapping position that corresponds to the release position in the wake's potential minimum effectively acts as an attractor: due to the parabolic shape of the electrostatic potential, final trapping positions ζ_f of individual slices outside the potential minimum are clustered close behind the trapping position corresponding to the potential minimum. When designing plasma photocathodes, one may

take the parabolic profile of the trapping potential into account in more detail: for example, a symmetric release volume around the trapping minimum will lead to a folding of two regions around the minimum onto the same trapping positions whereas releasing slices only on one side of the minimum results in unique trapping positions. Releasing farther away from the minimum means an increasingly larger spread of trapping positions, and therefore a larger energy spread, longer bunch duration and reduced current. With regard to the witness beam charge, in this scan, excellent stability is seen. First, it is worthwhile to mention that all released witness electrons are trapped and form the witness bunch in this scenario, corresponding to a 100% charge capture efficiency. This is not necessarily trivial for someone unfamiliar with the Trojan Horse scheme, since charge efficiency during injection or staging is a significant
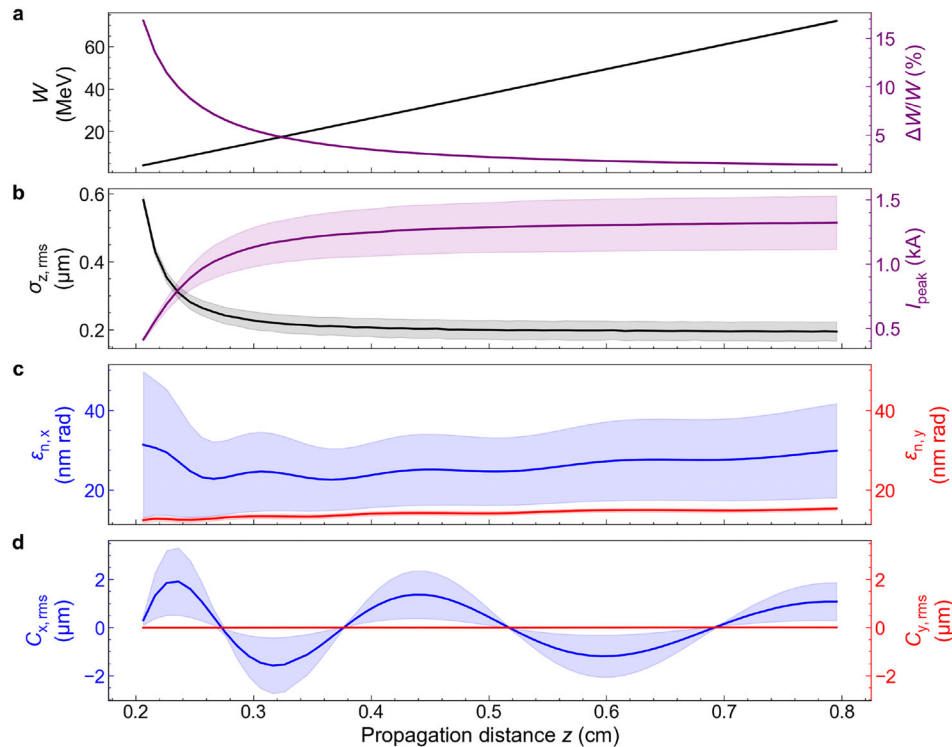
**ADVANCED
SCIENCE NEWS**

www.advancedsciencenews.com

annalen
der **physik**

www.ann-phys.org

Figure 15. Evolution of witness bunch parameters versus transverse jitter of collinear plasma photocathode laser pulse release position. From top to bottom, the evolution of energy gain W (left y-axis), relative energy spread $\Delta W/W$ (right y-axis), the resulting witness bunch length $\sigma_{z,\text{rms}}$ (left y-axis), peak current I_{peak} (right y-axis), normalized emittance $\epsilon_{n,x}$ in x-direction and the other transverse plane $\epsilon_{n,y}$, and witness beam centroid $C_{x,y,\text{rms}}$ in both planes are plotted as a function of propagation distance z.

challenge in other approaches such in staged LWFA[76] or via external injection from a linac.[77]

In absolute numbers, the injected charge here amounts to $Q \approx 2.375 \pm 0.006$ pC across the parameter sweep. The temporal jitter does not have a significant impact on the released charge because the electric wakefields close to the blowout centre are approximately zero; they hence do not contribute significantly to the tunneling ionization yield of the laser, as pointed out in ref. [27]. The excellent charge stability with jitters at the sub-percent level is a result of the decoupling of wakefield excitation and injection, enabled and controlled by the plasma photocathode.[27] At the same time, the bunch length $\sigma_{z,\text{rms}} \approx 0.22 \pm 0.04$ μm (r.m.s.) and the corresponding peak current $I_{\text{peak}} \approx 1.23 \pm 0.21$ kA in this configuration reflects the auto-compression features as discussed: the substantial longitudinal release position variation is compensated by the inherently forgiving trapping mechanism. With regard to emittance, excellent average values and excellent stability is obtained in this scan, amounting to $\epsilon_{n,x} \approx 15.11 \pm 0.13$ and $\epsilon_{n,y} \approx 15.51 \pm 0.12$ nm rad, respectively (see Figure 14c). Same holds for the centroid variation as shown in Figure 14d) and the magnitude of the centroid amplitude is of the order of sub-0.1 μm.

4.4. Transverse Injector Laser Shift

Next, the impact of a transverse injector laser jitter is regarded, based on the same default simulation setting as in the above sec-

tion. Stability toward transverse release position jitter variation was likewise first shown in ref. [22]. **Figure 15** shows details of the parameter evolution when the laser pulse is shifted by up to $\Delta X_{\text{Laser}} = 10$ μm. The solid lines represent the average value over all simulations performed in 2 μm-steps up to the maximum ΔX_{Laser} shift, and the shading again shows the standard deviation interval around the baseline. The maximum shift X_{Laser} corresponds to $\approx 15\%$ of the maximum plasma blowout radius $R_b = 65$ μm. While the absolute parameter scan range of 10 μm is very similar to the longitudinal (temporal) scan range, the relative change of release position within the blowout is much larger in this scan, due to the elliptic shape of the plasma wave blowout. Nevertheless, similar or better stability level as for the temporal jitter scan is seen for witness beam energy, energy spread, charge, and peak current (also see summary Table 1). For example, the witness beam charge stability amounts to $Q \approx 2.371 \pm 0.005$ pC across the parameter sweep. As for the longitudinal jitter, the transverse wakefields do not contribute significantly to the charge yield jitter, as known from ref. [27].

The variation of emittance in x-direction is larger than in y-direction, as expected from an off-axis release position in x-direction because of the larger transverse momenta of the electrons. Nevertheless, it amounts to $\approx 29.91 \pm 11.8$ nm rad—these are values that are even in a worst-case scenario better than from state-of-the-art linacs by orders of magnitude. At the LCLS linac, for example, the (simulated) normalized emittance of the electron beam is of $\approx$ mm mrad-scale, and its shot-to-shot variation is of ≈ 0.5 mm mrad-scale.[78,79] This suggests that not only the

2200655 (16 of 26)

**ADVANCED
SCIENCE NEWS**

www.advancedsciencenews.com

annalen
der **physik**

www.ann-phys.org

average emitance can be by a factor of ≈ 100 better than state-of-the-art, but also the emittance stability of the plasma photocathode may be 10 times better than at the best X-FEL linacs today. Of course, one may argue that a comparison between simulations with variations of only a few parameters with full-scale experimental results would be inherently unfair and that many experimental milestones are to be reached yet; however on the other hand, as explained earlier the combination of plasma photocathode, bunch compressor and accelerator within a single stage conceptually simplifies the setup substantially when compared to a state-of-the-art linac. The inherent robustness of the plasma photocathode with regard to physical principles, and the overall simplicity of the setup, may allow bringing inherent stability and controllability prospects to fruition.

Electrons released off-axis experience the restoring force of the ion background in the x-direction. This excites collective transverse oscillations of the witness beam electrons only in the x-direction, apparent from the centroid evolution plotted in Figure 15d). However, it can be seen that the oscillation amplitudes quickly decrease with increasing beam energy. Already at a witness beam energy of $W \approx 70$ MeV reached at the end of the 0.8 cm propagation distance, the witness beam centroid amplitude reaches the μm to sub-μm-level, and will be further reduced with increasing beam energy. Again, this is an important intrinsic advantage of releasing electrons at rest inside the wake. Inherently, off-axis injected beams from plasma photocathodes will rapidly self-align to the driver beam propagation axis with increasing beam energy and therefore, alignment of the driver beam to the desired orbit is the primary challenge in minimizing centroid jitter of the witness beam at the plasma stage exit. This rapid reduction of the betatron oscillation is of multi-faceted advantage. Perhaps most strikingly, one may compare the situation with external injection of pre-accelerated electron beams. In such a scenario, where the electron beam may have an energy of already tens or hundreds of MeV at the point of injection, a transverse, or even worse an angular pointing jitter can be catastrophic and may result in full or partial beam charge loss. Even if eventually the relativistic injected beam is captured in the plasma wake, it will perform betatron oscillations with large amplitude over a much longer distance. It will also not move to a favorable accelerating phase automatically, in contrast to electrons released at rest by a plasma photocathode laser. A centroid offset and oscillation of the witness beam is not only problematic inside a plasma accelerator stage but imposes fundamental challenges for beam transport post plasma, including complete beam loss due to a pointing exit angle outside the acceptance of the beam transport line. Next to partial or complete witness beam loss, hosing instabilities[80,81] and beam energy spread and bunch duration growth during the acceleration[82] are also unwanted. The plasma photocathode is a powerful approach to mitigate these issues.

4.5. Injector Laser Intensity Fluctuations

Laser pulse energy or power fluctuations will result in variation of the plasma photocathode laser pulse intensity at the injection position. Other factors such as spot size, wavefront flatness etc. also can vary from shot-to-shot, and will also effectively result in an intensity variation. In turn, laser pulse intensity fluctuations will

result in variation of the effective tunneling ionization yield. The impact of laser intensity on plasma photocathode injection was previously studied.[27,34,71] Notably already in ref. [27], not only the injector laser intensity was varied in simulations, but also the laser pulse spot size and duration, and the impact on emittance and brightness was explored. Laser intensity had been identified as a key parameter that can also be experimentally easily tuned, simply by changing the laser pulse energy. On the other hand, unwanted shot-to-shot jitters may also have a significant effect on the resulting witness beam. Again, PIC simulations around the baseline interaction parameter set can provide further insight into the behavior at a given working point. Using the baseline interaction parameter set, here the dimensionless laser amplitude a_0 was varied by up to $\pm 2\%$ around the baseline value of $a_0 = 0.018$, while keeping other laser parameters constant.

Figure 16 summarizes the impact of the laser intensity scan at this working point. Again, very high output parameter stability around outstanding average parameter values are obtained. With regard to output witness beam energy, the energy slightly decreases monotonically as the plasma photocathode laser intensity increases. The relative energy spread, in contrast, slightly increases monotonically as laser intensity increases. These trends can be attributed to beam loading as more charge is released and trapped when the release laser intensity increases (the released charge Q is given in the bottom left panel), and to the longer and larger release volume, which results in a longer beam and larger energy gain differences between head and tail of the beam, as known from ref. [40]. This systematic behavior means that the energy spread can be adjusted by tuning the laser pulse energy at the percent level, which is experimentally straightforward. Again, it may be worthwhile to highlight that even in a scenario where the laser energy and intensity may not be fully controllable to a_0 better than $\pm 2\%$, the energy stability of the output witness beams $W \approx 71.69 \pm 0.68$ MeV, and likewise, the relative energy spread of $\Delta W/W \approx 1.38 \pm 0.15\%$ are very promising, with slice energy spreads far below this level.

The normalized emittance in both planes (top right panel in Figure 16) increases monotonically with increasing laser intensity. Various factors contribute to this: first, a higher a_0 means that a larger volume of He gas is ionized, as a larger laser pulse electric field means higher ionization rates, and hence He electron release also occurs farther away from axis, which increases the initial transverse phase space of the witness beam. Second, larger a_0 also means electrons are released over a longer spread in longitudinal direction, which increases the range of betatron oscillation phases which contribute to the final trapped bunch (phase mixing). Third, higher bunch charge implies larger intrabunch space charge forces, which also slightly increase transverse electron momenta. And finally, larger a_0 will also increase the residual transverse momentum slightly, which also contributes to the finally obtained emittance. This thermal emittance contribution is estimated to be typically negligible when compared to the other sources of emittance, which justifies modeling the photocathode laser pulse with an envelope function instead of fully resolving it. A comparative analysis of the different sources of emittance in relevant scenarios and balanced optimization pathways shall be undertaken in further studies.

The charge yield Q (bottom left panel) shows significant changes over the full range of a_0 variation, as expected.[27] It shall

**ADVANCED
SCIENCE NEWS**

www.advancedsciencenews.com
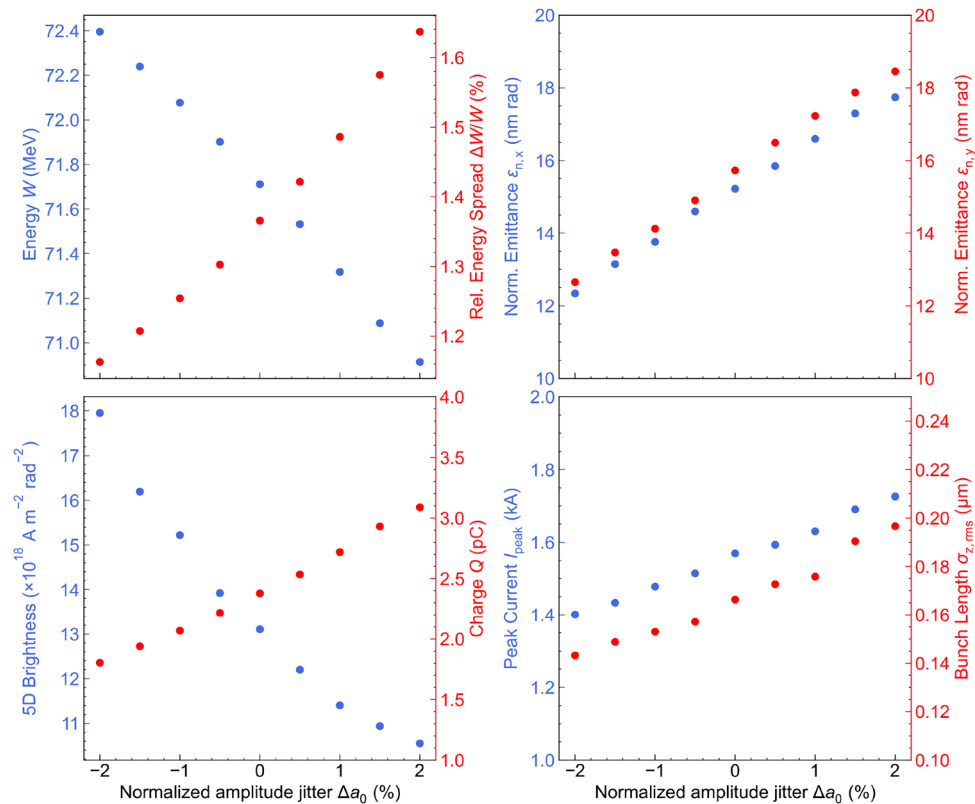
**annalen
der physik**

www.ann-phys.org

Figure 16. Condensed summary plot of key witness bunch parameters when scanning the effect of laser pulse intensity variations by varying a_0.

be noted that energy stability of sub-mJ class lasers can be substantially better than the range considered here, which in turn allows a much smaller charge jitter than considered here. For many applications, including key ones such as plasma-based X-FELs,[72] beam current is more important than charge. It is therefore of considerable interest that at the same time as the charge yield may increase due to higher a_0, also the bunch duration increases (bottom right panel). The associated current therefore by far does not increase as much as the charge, because the witness bunch duration increases with increasing charge. This auto-current-stabilization feature is then also inherited by the obtained brightness, another key performance parameter, for example, for FEL and other light source applications.

4.6. Overview of Impact of Timing, Transverse, and Intensity Jitter

As a composite parameter, the witness beam brightness not only reflects key beam parameters but can as well be used for quantifying overall beam stability. Parameter scans of beam brightness were first done in ref. [27]. Here, the impact of the three main jitter sources on the beam brightness for the given working point is compared in **Figure 17**.

In the left panel, impact of timing jitter between release laser pulse and blowout structure is presented, whereas the middle panel shows the impact of transverse jitter. Although 30 fs is approximately equivalent to the transverse jitter range of 10 μm,

the resulting 5D-brightness values (both mean and range) from the timing jitter study are even better than those obtained in the transverse jitter scan. The modest impact on beam brightness compared to the other jitter sources is expected, because of the quadratic contribution of emittance $B_{5D} \propto \epsilon_n^{-2}$ and the previously described outstanding resilience of emittance versus timing jitter. In summary, three factors are responsible for this. First, the elliptically shaped blowout has its principal axis in longitudinal direction, which as shown in Figure 13, means that the same absolute offset amounts to a relative offset which is smaller in the longitudinal direction of the elliptical blowout structure than in the transverse direction. Second, and more fundamentally consequential, the longitudinal electrostatic potential of the wake has a parabolic profile and a local minimum around the blowout centre (see Figure 13). Therefore, this release region is particularly resilient against longitudinal release position jitter as discussed above. Finally, the transverse momentum of electrons released at slightly different longitudinal positions is very similar. All these factors contribute to a substantially better emittance than obtained for the transverse offset scenario. This is a fortunate constellation, as at linac-driven systems the pointing stability of a laser pulse (the transverse jitter) is typically better controllable (e.g., to the few μm-scale[83]) than timing. The inherent larger resilience of the plasma photoinjector to timing than to transverse offset is therefore a complementary advantageous fit to the poorer timing precision when compared to the transverse precision in linac-based systems. For completeness, in the right panel of Figure 17 again the a_0-dependency of the 5D-brightness
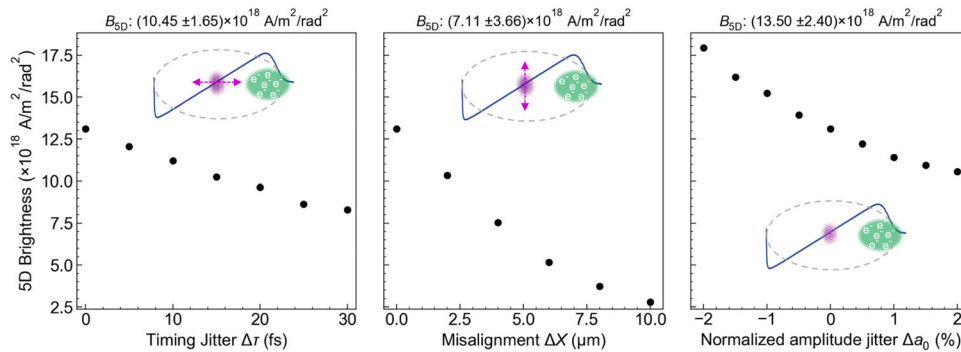

Figure 17. 5D-brightness dependency of plasma photocathode timing release variation (left), transverse plasma photocathode release position offset ΔX (middle), and of normalized amplitude a_0 of the plasma photocathode laser pulse.
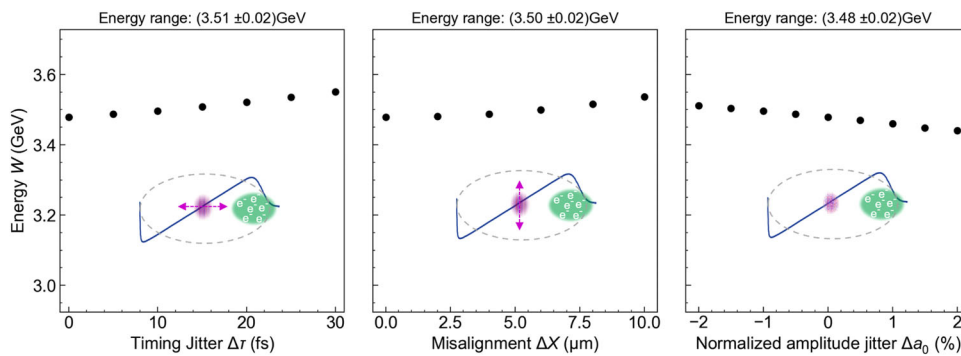

Figure 18. Electron energy dependency of plasma photocathode timing release variation (left), of transverse plasma photocathode release position offset ΔX (middle), and of normalized amplitude a_0 of the plasma photocathode laser pulse.

is presented, a plot corresponding to the one in Figure 16, bottom left panel.

Electron beams with unprecedented 5D-brightness are a central capability of the Trojan Horse plasma photocathode technique. The above summarized considerations and simulations indicate that at the same time there are also extremely attractive prospects with regard to the stability and tunability of such output electron beams. This may be perceived as counter-intuitive since conventional wisdom is rather that improvements in beam quality can be obtained mainly through higher complexity of the setup, which in turn puts much higher demands on technology control on aggregate.

Next to stability, for example, of the emittance and 5D-brightness, a further important aspect is the output energy stability. This is important for applications, for example when aiming at an FEL, where the electron beam energy defines the resonant wavelength of the produced radiation. Energy stability is also crucial for electron beam transport from the end of the plasma stage toward the applications. The energy stability of output witness beams with respect to the three jitter sources discussed above is therefore important. Again, PIC-simulations over the initial, and defining phase of acceleration (here, over 8 mm) can be used to quantify (output) energy by projecting the central energy gain, here up to $W \approx 3.5$ GeV. For simplicity, once may assume a non-evolving, constant wakefield, which is justified in the case of highly relativistic, high current driver beams such as available at SLAC.

Figure 18 summarizes the impact of the main jitter sources for the regarded working point showcase. When the timing is varied in longitudinal jitter scans (left panel of Figure 18), a release position longitudinally outside the electrostatic potential minimum means a trapping position further behind in the wakefield, hence a slightly larger energy gain.

When the transverse release position is shifted, the obtained energy actually also shows a slightly larger energy gain than when electrons are released on axis. When electrons are released off axis, they are performing said betatron oscillations around the axis, leading to reduction of the longitudinal velocity during the trapping process due to the relativistic momentum conservation. Therefore, electrons require longer acceleration distances to catch up with the plasma wave and are trapped further at the rear of the wakefield. The same point can be expressed by arguing with a smaller electrostatic wake potential outside the blowout center (see Figure 13).

Hence, the accelerating longitudinal wakefields at the corresponding trapping positions (see the blue profile in the schematic insets in Figure 18) for offset release are slightly larger than at a trapping position earlier in the wake. One could aim at maximum energy gain by releasing at a position that ensures the latest possible trapping position, but one may prefer to factor in a safety margin as regard the witness beam trapping position as done for the working point considered here. This is another advantage of the scheme: the electron driver beam will in practice have energy and current jitter, and the plasma wakefield will evolve due

**ADVANCED
SCIENCE NEWS**

www.advancedsciencenews.com

**annalen
der physik**

www.ann-phys.org

to driver beam energy depletion, head erosion, etc. By allowing a sufficient safety margin and not aiming to trap at the very end of the initial wakefield distribution, one can effectively ensure that the electron witness beam is stably accelerated in a "safe zone" of the wakefield.

Finally, the a_0-dependency is scanned (right panel of Figure 18). Here, it is observed that when the laser amplitude increases, the energy gain is decreasing—as discussed before, this can be attributed to slight beam loading when a stronger laser pulse releases more charge (and current).

In total, the resulting energy stability across all these scans is excellent: the energy variation amounts to the sub-1% level. This is a level similarly obtained at state-of-the-art linacs which drive X-FELs.[78,79]

Table 1 summarizes the jitter of witness beam parameters with respect to spatiotemporal and intensity jitter of the injector laser around the baseline scenario. We note that the plasma photocathode spatiotemporal pointing jitter of incoming beams measured at FACET (see Figure 10) is of the same order of magnitude as the jitter assumed here. However, today's technical capability for jitter minimization of incoming beams is much better than that (e.g., at FACET-II efforts are made to improve those), so we conclude that jitters as assumed here, even if, for example, longer propagation of the laser pulse in plasma in case of collinear injector geometry represents an additional challenge, are entirely possible, and likely can be much better. This further enhances prospects for improved stability of output beams.

The impact of shot-to-shot variations of the driver beam parameters on the PWFA, which in turn may have significant impact also on the produced witness beam, is not explored in detail in the reviewed plasma photocathode references such as.[21,22,27,33,34,71] That said, it was pointed out that due to the decoupling of injection and wake excitation, in contrast to other schemes the impact of driver beam variation on the witness beam is expected to be much reduced compared to other schemes where even the injection rate is strongly dependent on the wakefield structure. Nevertheless, jitter studies of the driver beam, based on simulated or measured incoming driver beam stability data, for example, at FACET-II or hybrid plasma wakefield accelerators, should in the future be fed into more realistic start-to-end simulations to describe the experimental real-world scenarios with increasing accuracy.

5. Brightness Preservation and Plasma-X-FEL Applications

The generation of ultrabright beams within the plasma not necessarily means that the beams survive extraction from the plasma, and the transport toward applications without loss of beam quality. A fundamental challenge is that electron beams in plasma wakefields are very strongly focused by the ion background. When the plasma ends, this focusing background vanishes, and the electron beams exit into the vacuum with a comparatively large divergence. One may draw an analogy to focusing of light, where a small focal spot size implies a short Rayleigh length and large divergence of the diffracting beam. As with light, one may be able to capture and refocus the strongly divergent beam with suitable optics, but chromatic aberration then may destroy the

emittance and brightness of the beam. This is a significant issue already at normalized emittance levels of the order of 1 mm-mrad, and for experimental scenarios emittance growth during extraction and transport may be of the same level. Such emittance growth would be orders of magnitude larger than the few tens of nm-rad normalized emittance levels that are supported by plasma photocathodes, and hence would eliminate this emittance advantage. If beams have lower energy spreads, chromatic aberrations and emittance growth during transport can be reduced. Low energy spreads are also required for many applications, including demanding ones such as X-ray free-electron-lasers.

Various approaches exist for energy spread reduction within or after the plasma stage,[84–91] however, schemes that achieve energy spread reduction post-plasma and during staging, aim at being compatible with electron beams with mm-mrad-level normalized emittance, not with beams that have nm-rad-level emittance. In ref. [40] it was found, that in order to preserve emittance and brightness of nm-rad-level electron beams from plasma photocathodes, one has to achieve energy spread compensation directly within a single plasma accelerator stage. While direct beam loading and flattening of the accelerating electric wakefield at the trapping position of the beam is possible by increasing the charge released by the plasma photocathode, operation in the high-charge regime of plasma photocathodes suffers from space charge-based emittance growth to some extent.

The lowest emittances and highest brightnesses can be reached by the so-called "escort"-beam-based approach invented in ref. [40]. In this method, the high-brightness witness beam is produced first, and beam loading is introduced only later within the plasma stage by adding a high-charge escort beam, when the witness beam is already accelerated to higher energies and is then largely immune to space charge. This allows tunable dechirping of the bright witness beam, while preserving its ultra-low emittance. Consequently, at the optimum dechirping point, when the energy chirp of the witness beam is maximally removed, the witness beam has maximized 6D brightness.

Figure 19 shows the evolution of witness beam energy, absolute (relative) energy spread and energy chirp after the escort bunch is released and trapped, using the reference case established in ref. [40]. The solid lines indicate the baseline case, and the shaded region indicates the confidence band resulting from potential misalignment or shot to shot jitter of the plasma photocathode laser pulse by up to 8 µm in the transverse direction. The reversed wakefield gradient at the witness (and escort) beam trapping position initiates the dechirping. Optimum dechirping is reached at $z \approx 2.4$ cm. Beyond that point, the energy spread increases again because the witness beam starts developing a positive energy chirp. The optimum dechirping point is the desired position to extract the beam from the plasma stage. Similar to Section 4.4, the study in ref. [30] suggests that misalignment of the dechirper plasma photocathode laser pulse may have a negligible impact on the optimum dechirping point and corresponding resulting energy spread and brightness of the witness. This implies that the stability of beam parameters discussed in the previous sections also applies to the escort-beam-based dechirping scheme. This combination of ultra-high brightness beam injector and dechirper alongside with the stabilization mechanisms are key building blocks toward full preservation of beam quality
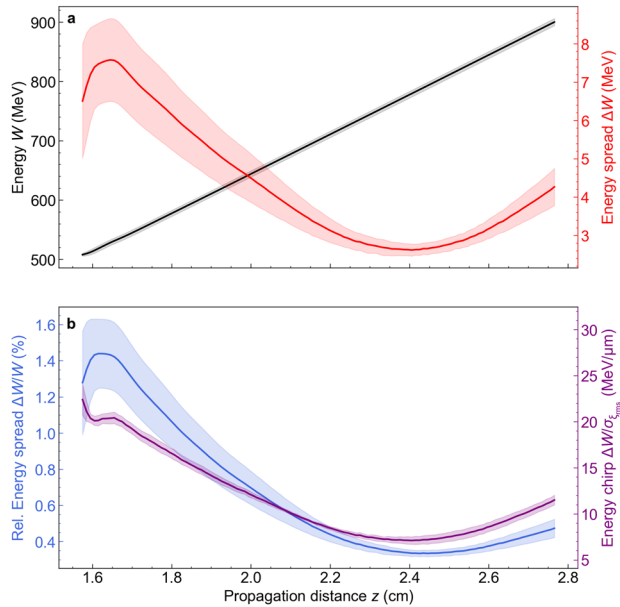
Figure 19. Escort beam-based dehchirping and impact of plasma photocathode misalignment on the dechiping efficiency of the witness beam. Data taken from ref. [30, 40].

at the nm-rad scale, and the realization of most demanding applications such as a hard X-FEL.

These innovations may enable the realization of multi-GeV electron beams with extreme 6D brightness values of the order of $\mathcal{O}(10^{19} \text{A}/\text{m}^2 \text{rad}^2 \, 0.1\%\text{BW})$ with normalized emittances at the 10's of nm-rad scale and sub-0.1% relative energy spreads, their successful extraction from the plasma stage, and transport into a X-FEL-capable undulator without any brightness loss.[72] **Figure 20** summarizes the evolution of the average slice normalized emittance and relative energy spread along the three building blocks of a plasma-X-FEL in a high-fidelity start-to-end simulation.[72] The plasma photocathode PWFA stage hosts the generation, acceleration, escort-based dechirping, and extraction of the ultra-high 6D brightness beam from the plasma stage
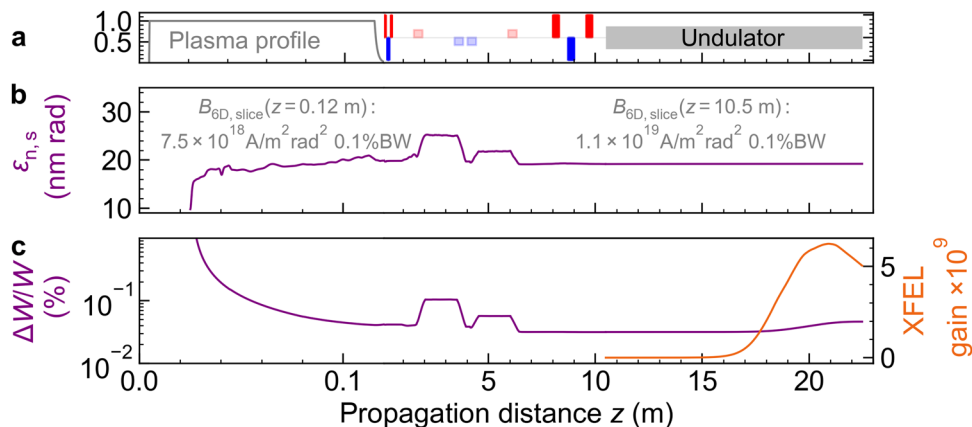
with nm-rad level normalized emittance preservation. Next, a subsequent beam transport line captures (permanent-magnet quadrupole triplet), isolates (chicane) and focuses (electromagnet quadrupole triplet) the ultra-high 6D brightness witness beam into an undulator without charge and quality loss. Here, the electron beam is orders of magnitude brighter than in conventional X-FELs, suffices the FEL emittance and energy spread thresholds already at comparatively low energy, and then develops ultrahigh photon pulse gain inside undulators, due to its brightness. Already at 2.7 GeV energy as chosen as working point in ref. [72], such a witness beam produces powerful coherent X-ray pulses at sub-Ångstrom wavelength and with attosecond duration, with saturation reached potentially already after 10 m of the undulator section.

Summarizing, the studies conducted for ref. [40, 72] have shown, that generation, and complete preservation of ultrabright beams from plasma photocathodes during extraction and transport may be possible, and that applications such as ultrahigh-quality, hard X-FELs could be powered by these beams.

6. Conclusion and Outlook

The plasma photocathode approach extends the exploitation of plasma 'merely' as an accelerator module with superior gradients to also being a source of electron beams with superior characteristics. In this work, we introduce the concept in context of the challenges of conventional electron accelerators, followed by a review of the E-210: Trojan Horse experiment at FACET[21] and a discussion of limitations of this experiment, together with formulating improvement measures and techniques that will be aimed at further versions of plasma photocathodes at FACET-II and beyond. The influence of key jitter sources is reviewed in detail, accompanied with a forward-looking discussion on attainable jitter resilience, showing that extraordinary stability may be achieved for suitable working points.

The preionized plasma channel is an important bottleneck that has to be widened to allow unconstrained PWFA to be performed. Step-like tunneling ionization thresholds of gaseous media with low and high ionization thresholds can then be harnessed to provide an ionization intensity corridor feature that offers resilience

Figure 20. Slice normalized emittance (b, purple line) and relative energy spread (c, purple line) evolution along the three bulding blocks (a) of the plasma-X-FEL and corresponding X-FEL gain (c, orange line). Reproduced under the terms of the CC-BY 4.0 license.[72] Copyright 2023 Crown, published by Springer Nature.

**ADVANCED
SCIENCE NEWS**

www.advancedsciencenews.com

annalen
der **physik**

www.ann-phys.org

toward shot-to-shot preionization laser pulse jitters in terms of power and effective intensity and alignment. A wider channel also allows for operation at lower plasma density and correspondingly larger blowouts. This can solve a number of issues. For example, unwanted hot spots can be avoided, relative plasma photocathode spatiotemporal injection precision is improved, residual energy spread of injected electrons is decreased, and possible benefits for emittance and extraction can be harnessed. Additionally, better stability of incoming electron driver beam and injector laser pulse, and electron-to-laser pulse synchronization contributes to improved absolute injection precision.

We highlight two major thrusts: First, both the ultralow emittance and ultrahigh brightness potential of plasma photocathodes make them ideal candidates for photon sources such as soft X-ray coherent synchrotron radiation sources,[92,93] hard X-ray FEL,[66,72,94] betatron radiation and ion channel lasers,[65,66] and γ-ray sources.[66] Second, such beams could be exploited for R&D toward beam quality of high energy physics (HEP) colliders and for next-generation experiments probing quantum electrodynamics. The paramount importance of beam quality and in particular emittance and brightness for both thrusts is well-known,[95] and hence, for example, plasma-based X-FELs are seen as a major milestone and stepping stone toward high energy physics applications.[69,96] This strategic connection is true for various types of accelerator R&D, but it is epitomized for the plasma photocathode wakefield acceleration concept: ultralow emittance and ultrahigh brightness – the chief attraction of plasma photocathodes – is the key beam requirement for X-FELs,[22,95] for example, with regard to photon energy and gain, but also for high energy physics because of luminosity considerations.

The plasma photocathode-based X-FEL thrust is currently investigated in the PWFA-FEL[97] design effort as a UK-US collaboration. A most recent study showcases the prospects of exploiting ultrabright electron beams from plasma photocathodes for attosecond-Angstrom class X-FELs in an ultracompact setup.[72] Plasma photocathode beam brightness transformers are also considered as capability upgrades for existing X-FELs and for new X-FEL visions, for example, as an addition for the UK XFEL in its Science Case[98] – the first time plasma-based X-FEL is contributing to a scientific case right from its conception. Further, the potential availability of intense hard X-ray or γ-ray beams, derived from ultrabright electrons produced by integrated plasma photocathode wakefield accelerators via novel and/or improved mechanisms,[66,72] could enable innovative constellations for particle and photon colliders.

For HEP and particle colliders, in particular, ultrabright beams have several short- to long term applications. As mentioned already in ref. [95], one long-term prospect of ultralow emittance electron beams would be to open up the possibility of obviating the electron beam damping ring. But there are also many short-term applications, such as using ultralow emittance beams from plasma photocathodes as test beams for emittance preservation during staging. For a future TeV-class linear collider with many stages, for example, even a few nm-rad-scale emittance growth per stage could be prohibitive for reaching luminosity goals – therefore nm-rad-scale test beams are required. This is coupled with the task of nm-rad-scale emittance diagnostics, and other ultrabright electron beam diagnostics. Spin-polarized elec-

tron beams may also be possible from plasma photocathodes, for example, by using pre-polarized targets and/or ionization via (circularly) polarized laser pulses.[99–101] However, spin depolarization in strong plasma wakefields has to be considered.[102] Release laser pulses with arbitrary frequency and polarization direction, including circular polarization, are foreseen capabilities of the plasma photocathode,[24] and strong field ionization-based spin polarization was numerically explored in ref. [103].

The ultralow emittance combined with femtosecond-level bunch duration – corresponding to multi kA currents and linac-level energy spreads[66] – in principle also allows for extreme charge densities. The resulting collective, Lorentz-boosted unipolar electric field distribution is a unique modality, which makes them attractive, for example, for QED studies.[104]

Finally, efforts to use plasma also as collective diagnostics of low emittance and/or high brightness beams, for example, via the plasma afterglow[56] mechanism, and for symmetric focusing of such beams via plasma lenses[105–107] are highly synergistic with plasma photocathodes. The overacrhing aim of the plasma afterglow technique[56] as a highly sensitive detector medium is to retrieve important characteristics of electron and laser beams by harnessing the collective response of plasma with high sensitivity, but non-intrusively. Plasma afterglow light emission has previously been shown to be useful for energy transfer inside plasma.[108] The use of plasma as a high-sensitivity detector would then complete the trinity of plasma-based photoguns, accelerators and detectors. Jointly with plasma lenses and other plasma-based beam manipulation techniques,[109] we are therefore on the path to an emerging, mutually reinforcing ecosystem of plasma- and laser-based building blocks.

At FACET-II, an interconnected set of experiments will be used to explore and develop these approaches. This includes the E-310 to E-313 experiments series for electron beam generation and acceleration, and the E-315 and E-316 experiments for diagnostics.

In parallel, the hybrid LWFA→PWFA approach has been developed from concept[41] to an experimentally viable platform over the last decade,[42,43,110,111] and now is contributing to the forefront of PWFA R&D, with achieved milestones such as observation of ion motion via shadowgraphy,[42] first gas-dynamic density downramp injection in PWFA,[44] and all-optical shock front injection.[45] Among next milestones of this increasingly successful approach is plasma photocathode-based electron beam production. Partially, significantly different challenges than in linac-driven PWFA and plasma photocathode R&D have to be overcome in this approach, for example stability and divergence of the electron beam from LWFA. However the capability of inherently synchronized plasma photocathode laser pulses and electron beams emerging from these systems[22] is a fundamentally helpful asset suitable for longitudinally high-precision injection, operation at high plasma densities where required, multi-bunch production[39,40] and many other advantages.[43,111]

The experimental progress both on realization of plasma photocathodes as well as on compact LWFA→PWFA, and parallel progress toward light sources, for example, by start-to-end simulations of plasma-photocathode-based hard X-FEL,[72] allows envisioning experimental scenarios that combine these thrusts in co-located setups that open up completely new experimental possibilities. **Figure 21** shows a timeline that summarizes a bird's eye view on these prospects.
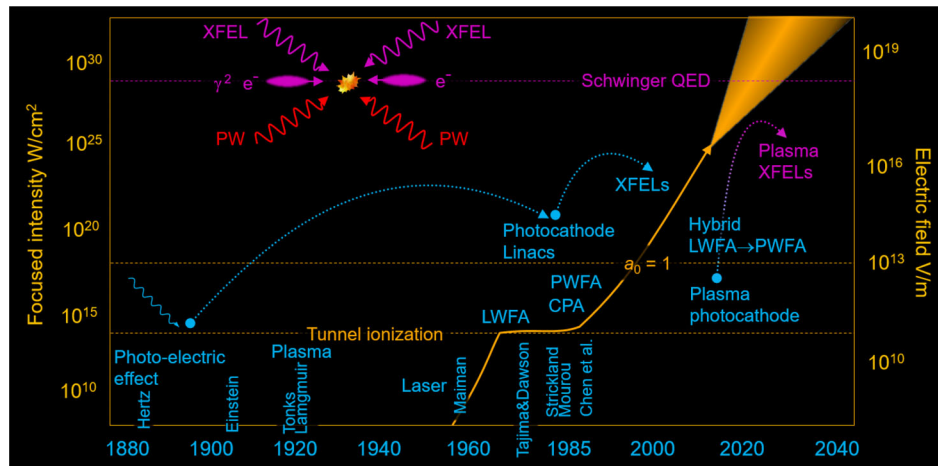
Figure 21. Timeline summarizing selected key developments and prospects with regard to improved photon and electron beam intensity and brightness, and resulting experimental capabilities.

In particular when based on compact LWFA→PWFA with intrinsic synchronization, the well-concerted, co-located interaction of multi-100 TW-class or PW-class laser pulses, ultrabright electron beams from plasma photocathodes, and hard X-FEL pulses or γ-pulses derived from these electron beams, with extreme intensities at the interaction point, may become possible. Such an example scenario is indicated in the top left of the diagram. This vision may sound futuristic from today's perspective, given that today hard X-FEL pulses can exclusively be produced by km-long linac-based setups, but so far both the experimental development of the plasma photocathode as well as the hybrid LWFA→PWFA is in remarkable agreement with theoretical expectations and simulations. If this trend continues, this vision may become increasingly realistic. The scientific questions that may become possible to address by such capabilities would include novel probing of matter and vacuum and exploration of questions pertinent, for example, to quantum electrodynamics, and myriad of other applications.

Acknowledgements

Conflict of Interest

The authors declare no conflict of interest.

Keywords

[1] H. Hertz, *Ann. Phys.* **1887**, *267*, 983.

[2] A. Einstein, *Ann. Phys.* **1905**, *322*, 132.

[3] A. Einstein, *Phys. Z.* **1917**, *18*, 124.

[4] T. H. MAIMAN, *Nature* **1960**, *187*, 493.

[5] C. Pellegrini, *Eur. Phys. J. H* **2012**, *37*, 659.

[6] P. Emma, R. Akre, J. Arthur, R. Bionta, C. Bostedt, J. Bozek, A. Brachmann, P. Bucksbaum, R. Coffee, F.-J. Decker, Y. Ding, D. Dowell, S. Edstrom, A. Fisher, J. Frisch, S. Gilevich, J. Hastings, G. Hays, Ph Hering, Z. Huang, R. Iverson, H. Loos, M. Messerschmidt, A. Miahnahri, S. Moeller, H. D. Nuhn, G. Pile, D. Ratner, J. Rzepiela, D. Schultz, et al., *Nat. Photonics* **2010**, *4*, 641.

[7] D. H. Dowell, J. F. Schmerge, *Phys. Rev. ST Accel. Beams* **2009**, *12*, 074201.

[8] E. Prat, S. Bettoni, H.-H. Braun, M. C. Divall, T. Schietinger, *Phys. Rev. ST Accel. Beams* **2015**, *18*, 063401.

[9] F. Zhou, D. Bohler, Y. Ding, S. Gilevich, Z. Huang, H. Loos, D. Ratner, S. Vetter, SLAC National Accelerator Lab., Menlo Park, CA, USA **2015**.

[10] S. Heifets, G. Stupakov, S. Krinsky, *Phys. Rev. ST Accel. Beams* **2002**, *5*, 064401.

[11] Z. Huang, K.-J. Kim, *Phys. Rev. ST Accel. Beams* **2002**, *5*, 074401.

[12] S. Di Mitri, *Phys. Rev. ST Accel. Beams* **2013**, *16*, 050701.

[13] S. Di Mitri, *Photonics* **2015**, *2*, 317.

[14] J. B. Rosenzweig, A. Cahill, B. Carlsten, G. Castorina, M. Croia, C. Emma, A. Fukusawa, B. Spataro, D. Alesini, V. Dolgashev, M. Ferrario, G. Lawler, R. Li, C. Limborg, J. Maxson, P. Musumeci, R.

Pompili, S. Tantawi, O. Williams, *Nucl. Instrum. Methods Phys. Res., Sect. A* **2018**, *909*, 224.

[15] R. J. England, P. Hommelhoff, R. L. Byer, *Phys. Today* **2021**, *74*, 42.

[16] T. Tajima, J. M. Dawson, *Phys. Rev. Letters* **1979**, *43*, 267.

[17] P. Chen, J. M. Dawson, R. W. Huff, T. Katsouleas, *Phys. Rev. Lett.* **1985**, *54*, 693.

[18] J. B. Rosenzweig, *Phys. Rev. Lett.* **1987**, *58*, 555.

[19] I. Blumenfeld, C. E. Clayton, F.-J. Decker, M. J. Hogan, C. Huang, R. Ischebeck, R. Iverson, C. Joshi, T. Katsouleas, N. Kirby, W. Lu, K. A. Marsh, W. B. Mori, P. Muggli, E. Oz, R. H. Siemann, D. Walz, M. Zhou, *Nature* **2007**, *445*, 741.

[20] M. Litos, E. Adli, W. An, C. I. Clarke, C. E. Clayton, S. Corde, J. P. Delahaye, R. J. England, A. S. Fisher, J. Frederico, S. Gessner, S. Z. Green, M. J. Hogan, C. Joshi, W. Lu, K. A. Marsh, W. B. Mori, P. Muggli, N. Vafaei-Najafabadi, D. Walz, G. White, Z. Wu, V. Yakimenko, G. Yocky, *Nature* **2014**, *515*, 92.

[21] A. Deng, O. Karger, T. Heinemann, A. Knetsch, P. Scherkl, G. Manahan, A. Beaton, D. Ullmann, G. Wittig, A. Habib, Y. Xi, M. D. Litos, B. D. O'Shea, S. Gessner, C. I. Clarke, S. Z. Green, C. A. Lindstrøm, E. Adli, R. Zgadzaj, M. C. DownerG. Andonian, A. Murokh, D. L. Bruhwiler, J. R. Cary, M. J. Hogan, V. Yakimenko, J. B. Rosenzweig, B. Hidding, *Nat. Phys.* **2019**, *15*, 5.

[22] B. Hidding, G. Pretzler, J. B. Rosenzweig, T. Königstein, D. Schiller, D. L. Bruhwiler, *Phys. Rev. Lett.* **2012**, *108*, 035001.

[23] B. Hidding, J. B. Rosenzweig, Y. Xi, B. O'Shea, G. Andonian, D. Schiller, S. Barber, O. Williams, G. Pretzler, T. Königstein, F. Kleeschulte, M. J. Hogan, M. Litos, S. Corde, W. W. White, P. Muggli, D. L. Bruhwiler, K. Lotov, *AIP Conf. Proc.* **2012**, *1507*, 570.

[24] B. Hidding, G. Pretzler, D. Bruhwiler, J. Rosenzweig, German Patent DE102011104858A1 **2011**, US Patent PCT/US12/043002.

[25] M. Ferrario, T. Katsouleas, L. Serafini, I. Zvi, *IEEE Trans. Plasma Sci.* **2000**, *28*, 1152.

[26] R. Lehe, M. Kirchen, I. A. Andriyash, B. B. Godfrey, J.-L. Vay, *Comput. Phys. Commun.* **2016**, *203*, 66.

[27] Y. Xi, B. Hidding, D. Bruhwiler, G. Pretzler, J. B. Rosenzweig, *Phys. Rev. ST Accel. Beams* **2013**, *16*, 031303.

[28] K. Floettmann, *Phys. Rev. ST Accel. Beams* **2003**, *6*, 034202.

[29] C. B. Schroeder, J.-L. Vay, E. Esarey, S. S. Bulanov, C. Benedetti, L.-L. Yu, M. Chen, C. G. R. Geddes, W. P. Leemans, *Phys. Rev. ST Accel. Beams* **2014**, *17*, 101301.

[30] G. G. Manahan, A. F. Habib, P. Scherkl, D. Ullmann, A. Beaton, A. Sutherland, G. Kirwan, P. Delinikolas, T. Heinemann, R. Altuijri, A. Knetsch, O. Karger, N. M. Cook, D. L. Bruhwiler, Z.-M. Sheng, J. B. Rosenzweig, B. Hidding, *Philos. Trans. R. Soc., A* **2019**, *377*, 20180182.

[31] M. Stumpf, M. Melchger, S. Montag, G. Pretzler, *J. Phys. B: At., Mol. Opt. Phys.* **2022**, *55*, 015401.

[32] N. Bourgeois, J. Cowley, S. M. Hooker, *Phys. Rev. Lett.* **2013**, *111*, 155004.

[33] B. Hidding, G. G. Manahan, O. Karger, A. Knetsch, G. Wittig, D. A. Jaroszynski, Z.-M. Sheng, Y. Xi, A. Deng, J. B. Rosenzweig, G. Andonian, A. Murokh, G. Pretzler, D. L. Bruhwiler, J. Smith, *J. Phys. B: At., Mol. Opt. Phys.* **2014**, *47*, 234010.

[34] F. Li, J. F. Hua, X. L. Xu, C. J. Zhang, L. X. Yan, Y. C. Du, W. H. Huang, H. B. Chen, C. X. Tang, W. Lu, C. Joshi, W. B. Mori, Y. Q. Gu, *Phys. Rev. Lett.* **2013**, *111*, 015003.

[35] L.-L. Yu, E. Esarey, C. Schroeder, J.-L. Vay, C. Benedetti, C. Geddes, M. Chen, W. Leemans, *Phys. Rev. Lett.* **2014**, *112*, 125001.

[36] D. Umstadter, J.-K. Kim, E. Dodd, US5789876 **1995**.

[37] M. W. von der Leyen, J. Holloway, Y. Ma, P. T. Campbell, R. Aboushelbaya, Q. Qian, A. F. Antoine, M. Balcazar, J. Cardarelli, Q. Feng, R. Fitzgarrald, B. X. Hou, G. Kalinchenko, J. Latham, A. M. Maksimchuk, A. McKelvey, J. Nees, I. Ouatu, R. W. Paddock, B. Spiers, A. G. R. Thomas, R. Timmis, K. Krushelnick, P. A. Norreys, *Phys. Rev. Lett.* **2023**, *130*, 105002.

[38] X. L. Xu, J. F. Hua, F. Li, C. J. Zhang, L. X. Yan, Y. C. Du, W. H. Huang, H. B. Chen, C. X. Tang, W. Lu, P. Yu, W. An, C. Joshi, W. B. Mori, *Phys. Rev. Lett.* **2014**, *112*, 035003.

[39] B. Hidding, O. Karger, G. Wittig, C. Aniculaesei, D. Jaroszynski, B. W. J. McNeil, L. T. Campbell, M. R. Islam, B. Ersfeld, Z.-M. Sheng, Y. Xi, A. Deng, J. B. Rosenzweig, G. Andonian, A. Murokh, M. J. Hogan, D. L. Bruhwiler, E. Cormier, *Plasma Phys.* **2014**, 1403.1109.

[40] G. Manahan, A. Habib, P. Scherkl, P. Delinikolas, A. Beaton, A. Knetsch, O. Karger, G. Wittig, T. Heinemann, Z. Sheng, J. Cary, D. Bruhwiler, J. Rosenzweig, B. Hidding, *Nat. Commun.* **2017**, *8*, 15705.

[41] B. Hidding, T. Koenigstein, J. Osterholz, S. Karsch, O. Willi, G. Pretzler, *Phys. Rev. Lett.* **2010**, *104*, 195002.

[42] M. F. Gilljohann, H. Ding, A. Döpp, J. Götzfried, S. Schindler, G. Schilling, S. Corde, A. Debus, T. Heinemann, B. Hidding, S. M. Hooker, A. Irman, O. Kononenko, T. Kurz, A. Martinez de la Ossa, U. Schramm, S. Karsch, *Phys. Rev. X* **2019**, *9*, 011046.

[43] T. Kurz, T. Heinemann, M. F. Gilljohann, Y. Y. Chang, J. P. Couperus Cabadağ, A. Debus, O. Kononenko, R. Pausch, S. Schöbel, R. W. Assmann, M. Bussmann, H. Ding, J. Götzfried, A. Köhler, G. Raj, S. Schindler, K. Steiniger, O. Zarini, S. Corde, A. Döpp, B. Hidding, S. Karsch, U. Schramm, A. Martinez de la Ossa, A. Irman, *Nat. Commun.* **2021**, *12*, 2895.

[44] J. P. Couperus Cabadağ, R. Pausch, S. Schöbel, M. Bussmann, Y.-Y. Chang, S. Corde, A. Debus, H. Ding, A. Döpp, F. M. Foerster, M. Gilljohann, F. Haberstroh, T. Heinemann, B. Hidding, S. Karsch, A. Koehler, O. Kononenko, A. Knetsch, T. Kurz, A. Martinez de la Ossa, A. Nutter, G. Raj, K. Steiniger, U. Schramm, P. Ufer, A. Irman, *Phys. Rev. Res.* **2021**, *3*, L042005.

[45] F. M. Foerster, A. Döpp, F. Haberstroh, K. v. Grafenstein, D. Campbell, Y.-Y. Chang, S. Corde, J. P. Couperus Cabadağ, A. Debus, M. F. Gilljohann, A. F. Habib, T. Heinemann, B. Hidding, A. Irman, F. Irshad, A. Knetsch, O. Kononenko, A. Martinez de la Ossa, A. Nutter, R. Pausch, G. Schilling, A. Schletter, S. Schöbel, U. Schramm, E. Travac, P. Ufer, S. Karsch, *Phys. Rev. X* **2022**, *12*, 041016.

[46] W. Lu, C. Huang, M. Zhou, W. B. Mori, T. Katsouleas, *Phys. Rev. Lett.* **2006**, *96*, 165002.

[47] A. Golovanov, I. Kostyukov, A. Pukhov, J. Thomas, *Quantum Electron.* **2016**, *46*, 295.

[48] J. Thomas, I. Y. Kostyukov, J. Pronold, A. Golovanov, A. Pukhov, *Phys. Plasmas* **2016**, *23*, 053108.

[49] A. Pukhov, *J. Plasma Phys.* **1999**, *61*, 425.

[50] A. Pukhov, presented at Proc. of the 2014 CAS–CERN Accelerator School: Plasma Wake Acceleration, Vol. 1, *CERN Yellow Reports* **2016**

[51] I. Kostyukov, A. Pukhov, S. Kiselev, *Phys. Plasmas* **2004**, *11*, 5256.

[52] L. Reichwein, J. Thomas, A. Golovanov, I. Kostyukov, A. Pukhov, *Plasma Phys. Control. Fusion* **2020**, *62*, 115017.

[53] T. N. Dalichaouch, X. L. Xu, A. Tableman, F. Li, F. S. Tsung, W. B. Mori, *Phys. Plasmas* **2021**, *28*, 063103.

[54] J. Pronold, J. Thomas, A. Pukhov, *Phys. Plasmas* **2018**, *25*, 123112.

[55] A. A. Golovanov, I. Y. Kostyukov, L. Reichwein, J. Thomas, A. Pukhov, *Plasma Phys. Control. Fusion* **2021**, *63*, 085004.

[56] P. Scherkl, A. Knetsch, T. Heinemann, A. Sutherland, A. F. Habib, O. S. Karger, D. Ullmann, A. Beaton, G. G. Manahan, Y. Xi, A. Deng, M. D. Litos, B. D. O'Shea, S. Z. Green, C. I. Clarke, G. Andonian, R. Assmann, D. L. Bruhwiler, J. Smith, J. R. Cary, M. J. Hogan, V. Yakimenko, J. B. Rosenzweig, B. Hidding, *Phys. Rev. Accel. Beams* **2022**, *25*, 052803.

[57] G. Wittig, O. Karger, A. Knetsch, Y. Xi, A. Deng, J. B. Rosenzweig, D. L. Bruhwiler, J. Smith, G. G. Manahan, Z.-M. Sheng, D. A. Jaroszynski, B. Hidding, *Phys. Rev. ST Accel. Beams* **2015**, *18*, 081304.

[58] D. Ullmann, P. Scherkl, A. Knetsch, T. Heinemann, A. Sutherland, A. F. Habib, O. S. Karger, A. Beaton, G. G. Manahan, A. Deng, G. Andonian, M. D. Litos, B. D. OShea, D. L. Bruhwiler, J. R. Cary, V. Hogan, M. J. Yakimenko, J. B. Rosenzweig, B. Hidding, *Phys. Rev. Res.* **2020**, *3*, 043163.

2200655 (24 of 26)

[59] Radiabeam: Plasma photocathode beam brightness transformer for laser-plasma-wakefield accelerators, DOE DESC0009533, 2013-2016, https://www.sbir.gov/sbirsearch/detail/407701.

[60] R. J. Shalloo, C. Arran, L. Corner, J. Holloway, J. Jonnerby, R. Walczak, H. M. Milchberg, S. M. Hooker, *Phys. Rev. E* **2018**, *97*, 053203.

[61] R. Zgadzaj, Z. Li, M. Downer, A. Sosedkin, V. Khudyakov, K. Lotov, T. Silva, J. Vieira, J. Allen, S. Gessner, M. J. Hogan, M. Litos, V. Yakimenko, *Nat. Commun.* **2020**, *11*, 4753.

[62] G. G. Manahan, A. Deng, O. Karger, Y. Xi, A. Knetsch, M. Litos, G. Wittig, T. Heinemann, J. Smith, Z. M. Sheng, D. A. Jaroszynski, G. Andonian, D. L. Bruhwiler, J. B. Rosenzweig, B. Hidding, *Phys. Rev. Accel. Beams* **2016**, *19*, 011303.

[63] C. Nieter, J. R. Cary, *J. Comput. Phys.* **2004**, *196*, 448.

[64] N. Barov, J. B. Rosenzweig, M. C. Thompson, R. B. Yoder, *Phys. Rev. ST Accel. Beams* **2004**, *7*, 061301.

[65] M. Litos, R. Ariniello, C. Doss, K. Hunt-Stone, J. R. Cary, presented at *2018 IEEE Adv. Accelerator Concepts Workshop (AAC)*, IEEE, Piscataway, NJ, USA **2018**, pp. 1–5.

[66] A. F. Habib, P. Scherkl, G. G. Manahan, T. Heinemann, D. Ullmann, A. Sutherland, A. Knetsch, M. Litos, M. Hogan, J. Rosenzweig, B. Hidding, in *Advances in Laboratory-Based X-Ray Sources, Optics, and Applications VII*, Vol. *11110*, International Society for Optics and Photonics, Bellingham, WA, USA **2019**, p. 111100A.

[67] K. Moon, S. Kumar, M. Hur, M. Chung, *Phys. Plasmas* **2019**, *26*, 073103.

[68] E. R. Colby, L. K. Len, *Rev. Accel. Sci. Technol.* **2016**, *09*, 1.

[69] B. Hidding, S. Hooker, S. Jamison, B. Muratori, C. Murphy, Z. Najmudin, R. Pattathil, G. Sarri, M. Streeter, C. Welsch, M. Wing, G. Xia, **2019**.

[70] J. Turner, R. Akre, A. Brachmann, F.-J. Decker, Y. Ding, P. Emma, Y. Feng, A. Fisher, J. Frisch, A. Gilevich, P. Hering, K. Horovitz, Z. Huang, R. Iverson, D. Kharakh, A. Krasnykh, J. Krzywinski, H. Loos, M. Messerschmidt, S. Moeller, H.-D. Nuhn, D. Ratner, T. Smith, J. Welch, J. Wu, presented at *Conf. Proc. C110328: 2423-2425, 2011*, SLAC-PUB-16660. SLAC National Accelerator Lab., Menlo Park, CA, USA, **2016**.

[71] R. Altuijri, P. Scherkl, T. Heinemann, A. Habib, A. Nutter, A. Hala, B. Hidding, presented at *46th EPS Conf. on Plasma Phys.*, EPS, Mulhouse, 2019, P5–2020.

[72] A. F. Habib, G. Manahan, P. Scherkl, T. Heinemann, A. Sutherland, R. Altuiri, B. M. Alotaibi, M. Litos, J. Cary, T. Raubenheimer, E. Hemsing, M. Hogan, J. Rosenzweig, P. H. Williams, B. W. J. McNeil, B. Hidding, *Nat. Commun.* **2023**, *14*, 1054.

[73] I. Kostyukov, A. Pukhov, S. Kiselev, *Phys. Plasmas* **2004**, *11*, 5256.

[74] E. Oz, S. Deng, T. Katsouleas, P. Muggli, C. D. Barnes, I. Blumenfeld, F. J. Decker, P. Emma, M. J. Hogan, R. Ischebeck, R. H. Iverson, N. Kirby, P. Krejcik, C. O'Connell, R. H. Siemann, D. Walz, D. Auerbach, C. E. Clayton, C. Huang, D. K. Johnson, C. Joshi, W. Lu, K. A. Marsh, W. B. Mori, M. Zhou, *Phys. Rev. Lett.* **2007**, *98*, 084801.

[75] A. Pak, K. A. Marsh, S. F. Martins, W. Lu, W. B. Mori, C. Joshi, *Phys. Rev. Lett.* **2010**, *104*, 025003.

[76] S. Steinke, J. van Tilborg, C. Benedetti, C. G. R. Geddes, C. B. Schroeder, J. Daniels, K. K. Swanson, A. J. Gonsalves, K. Nakamura, N. H. Matlis, B. H. Shaw, E. Esarey, W. P. Leemans, *Nature* **2016**, *530*, 190.

[77] Y. Wu, J. Hua, Z. Zhou, J. Zhang, S. Liu, B. Peng, Y. Fang, X. Ning, Z. Nie, F. Li, C. Zhang, C.-H. Pai, Y. Du, W. Lu, W. B. Mori, C. Joshi, *Nat. Phys.* **2021**, *17*, 801.

[78] P. Emma, in *Particle Accelerator Conference (PAC 09)*, **2010**, pp. TH3PBI01.

[79] M. Borland, Y. Chae, S. Milton, R. Soliday, V. Bharadwaj, P. Emma, P. Krejcik, C. Limborg, H. Nuhn, M. Woodley, in presented at *Proc. of the 2001 PAC, (Cat. No.01CH37268)*, Vol. 4, Chicago, IL, USA, **2001**, pp. 2707–2709.

[80] T. J. Mehrling, R. A. Fonseca, A. Martinez de la Ossa, J. Vieira, *Phys. Rev. Lett.* **2017**, *118*, 174801.

[81] A. M. de la Ossa, T. Mehrling, J. Osterhoff, *Phys. Rev. Lett.* **2018**, *120*, 144802.

[82] A. F. Pousa, A. M. de la Ossa, R. W. Assmann, *Sci. Rep.* **2019**, *9*, 1.

[83] P. Cinquegrana, S. Cleva, A. Demidovich, G. Gaio, R. Ivanov, G. Kurdi, I. Nikolov, P. Sigalotti, M. B. Danailov, *Phys. Rev. ST Accel. Beams* **2014**, *17*, 040702.

[84] T. Katsouleas, S. Wilks, P. Chen, J. Dawson, J. Su, *Part. Accel.* **1987**, *22*, 81.

[85] M. Tzoufras, W. Lu, F. S. Tsung, C. Huang, W. B. Mori, T. Katsouleas, J. Vieira, R. A. Fonseca, L. O. Silva, *Phys. Rev. Lett.* **2008**, *101*, 145002.

[86] R. Brinkmann, N. Delbos, I. Dornmair, M. Kirchen, R. Assmann, C. Behrens, K. Floettmann, J. Grebenyuk, M. Gross, S. Jalas, T. Mehrling, A. Martinez de la Ossa, J. Osterhoff, B. Schmidt, V. Wacker, A. R. Maier, *Phys. Rev. Lett.* **2017**, *118*, 214801.

[87] Y. Wu, J. Hua, Z. Zhou, J. Zhang, S. Liu, B. Peng, Y. Fang, Z. Nie, X. Ning, C.-H. Pai, Y. C. Du, W. Lu, C. J. Zhang, W. B. Mori, C. Joshi, *Phys. Rev. Lett.* **2019**, *122*, 204804.

[88] A. F. Pousa, A. M. de la Ossa, R. Brinkmann, R. Assmann, *Phys. Rev. Lett.* **2019**, *123*, 054801.

[89] V. Shpakov, M. Anania, M. Bellaveglia, A. Biagioni, F. Bisesto, F. Cardelli, M. Cesarini, E. Chiadroni, A. Cianchi, G. Costa, M. Croia, A. Del Dotto, D. Di Giovenale, M. Diomede, M. Ferrario, F. Filippi, A. Giribono, V. Lollo, M. Marongiu, V. Martinelli, A. Mostacci, L. Piersanti, G. Di Pirro, R. Pompili, S. Romeo, J. Scifo, C. Vaccarezza, F. Villa, A. Zigler, *Phys. Rev. Lett.* **2019**, *122*, 114801.

[90] R. D'Arcy, S. Wesch, A. Aschikhin, S. Bohlen, C. Behrens, M. J. Garland, L. Goldberg, P. Gonzalez, A. Knetsch, V. Libov, A. Martinez de la Ossa, M. Meisel, T. J. Mehrling, P. Niknejadi, K. Poder, J.-H. Röckemann, L. Schaper, B. Schmidt, S. Schröder, C. Palmer, J.-P. Schwinkendorf, B. Sheeran, M. J. V. Streeter, G. Tauscher, V. Wacker, J. Osterhoff, *Phys. Rev. Lett.* **2019**, *122*, 034801.

[91] R. Pompili, D. Alesini, M. Anania, M. Behtouei, M. Bellaveglia, A. Biagioni, F. Bisesto, M. Cesarini, E. Chiadroni, A. Cianchi, G. Costa, M. Croia, A. Del Dotto, D. Di Giovenale, M. Diomede, F. Dipace, M. Ferrario, A. Giribono, V. Lollo, L. Magnisi, M. Marongiu, A. Mostacci, L. Piersanti, G. Di Pirro, S. Romeo, A. R. Rossi, J. Scifo, V. Shpakov, C. Vaccarezza, F. Villa, et al., *Nat. Phys.* **2021**, *17*, 499.

[92] B. M. Alotaibi, R. Altuijri, A. Habib, A. Hala, B. Hidding, S. M. Khalil, B. McNeil, P. Traczykowski, *New J. Phys.* **2020**, *22*, 013037.

[93] C. Emma, X. Xu, A. Fisher, R. Robles, J. MacArthur, J. Cryan, M. Hogan, P. Musumeci, G. White, A. Marinelli, *APL Photonics* **2021**, *6*, 076107.

[94] C. Emma, J. Van Tilborg, R. Assmann, S. Barber, A. Cianchi, S. Corde, M. E. Couprie, R. D'Arcy, M. Ferrario, A. F. Habib, B. Hidding, M. J. Hogan, C. B. Schroeder, A. Marinelli, M. Labat, R. Li, J. Liu, A. Loulergue, J. Osterhoff, A. R. Maier, B. J. McNeil, W. Wang, *High Power Laser Sci. Eng.* **2021**, *9*, e57.

[95] K.-J. Kim, B. Carlsten, D. Dowell, K. Flottmann, K. Jensen, J. Petillo, A. Sessler, G. Stupakov, Towards advanced electron beam brightness enhancement and conditioning, Technical Report ANL/APS/LS-305, Argonne National Laboratory, **2004**, https://www.aps.anl.gov/files/APS-sync/lsnotes/files/APS_1418245.pdf.

[96] T. E. S. Group, Deliberation document on the 2020 Update of the European Strategy for Particle Physics, Technical Report CERN-ESU-014, Geneva **2020**, https://cds.cern.ch/record/2720131.

[97] B. Hidding, STFC PWFA-FEL: Exploratory study of PWFA-driven FEL at CLARA, **2019**, https://pwfa-fel.phys.strath.ac.uk/.

[98] J. Marangos, *Nat. Rev. Phys.* **2020**, *2*, 332.

[99] U. Fano, *Phys. Rev.* **1969**, *178*, 131.

[100] I. Barth, O. Smirnova, *Phys. Rev. A* **2013**, *88*, 013401.

[101] A. Hartung, F. Morales, M. Kunitski, K. Henrichs, A. Laucke, M. Richter, T. Jahnke, A. Kalinin, M. Schöffler, L. P. H. Schmidt, M. Ivanov, O. Smirnova, R. Dörner, *Nat. Photonics* **2016**, *10*, 526.

[102] J. Thomas, A. Hützen, A. Lehrach, A. Pukhov, L. Ji, Y. Wu, X. Geng, M. Büscher, *Phys. Rev. Accel. Beams* **2020**, *23*, 064401.

[103] Z. Nie, F. Li, F. Morales, S. Patchkovskii, O. Smirnova, W. An, N. Nambu, D. Matteo, K. A. Marsh, F. Tsung, W. B. Mori, C. Joshi, *Phys. Rev. Lett.* **2021**, *126*, 054801.

[104] V. Yakimenko, S. Meuren, F. Del Gaudio, C. Baumann, A. Fedotov, F. Fiuza, T. Grismayer, M. J. Hogan, A. Pukhov, L. O. Silva, G. White, *Phys. Rev. Lett.* **2019**, *122*, 190404.

[105] P. Chen, S. Rajagopalan, J. Rosenzweig, *Phys. Rev. D* **1989**, *40*, 923.

[106] P. Chen, K. Oide, A. M. Sessler, S. S. Yu, *Phys. Rev. Lett.* **1990**, *64*, 1231.

[107] C. Doss, E. Adli, R. Ariniello, J. Cary, S. Corde, B. Hidding, M. Hogan, K. Hunt-Stone, C. Joshi, K. Marsh, J. Rosenzweig, N. Vafaei-Najafabadi, V. Yakimenko, M. Litos, *Phys. Rev. Accel. Beams* **2019**, *22*, 11.

[108] E. Oz, C. D. Barnes, C. E. Clayton, F. J. Decker, S. Deng, M. J. Hogan, C. Huang, R. Iverson, D. K. Johnson, C. Joshi, T. Katsouleas, P.

Krejcik, W. Lu, K. A. Marsh, P. Muggli, C. O'Connell, D. Walz, *AIP Conf. Proc.* **2004**, *737*, 708.

[109] G. Wittig, O. S. Karger, A. Knetsch, Y. Xi, A. Deng, J. B. Rosenzweig, D. L. Bruhwiler, J. Smith, Z.-M. Sheng, D. A. Jaroszynski, G. G. Manahan, B. Hidding, *Nucl. Instrum. Methods Phys. Res., Sect. A* **2016**, *829*, 83.

[110] S. Schöbel, R. Pausch, Y.-Y. Chang, S. Corde, J. C. Cabadağ, A. Debus, H. Ding, A. Döpp, F. M. Foerster, M. Gilljohann, F. Haberstroh, T. Heinemann, B. Hidding, S. Karsch, A. Köhler1, O. Kononenko, T. Kurz, A. Nutter1, K. Steiniger, P. Ufer1, A. Martinez de la Ossa, U. Schramm, A. Irman, *New J. Phys.* **2022**, *24*, 083034.

[111] B. Hidding, R. Assmann, M. Bussmann, D. Campbell, Y.-Y. Chang, S. Corde, J. C. Cabadağ, A. Debus, A. Döpp, M. Gilljohann, J. Götzfried, F. M. Foerster, F. Haberstroh, F. Habib, T. Heinemann, D. Hollatz, A. Irman, M. Kaluza, S. Karsch, O. Kononenko, A. Knetsch, T. Kurz, S. Kuschel, A. Köhler, A. M. d. l. Ossa, A. Nutter, R. Pausch, G. Raj, U. Schramm, S. Schöbel, et al., *Photonics* **2023**, *10*, 99.

Fahim Habib a research associate at the University of Strathclyde, UK, has been involved in the E-210 project at SLAC FACET and continues to work on realizing high-brightness beams via plasma photocathodes at SLAC FACET-II. As lead researcher of the STFC PWFA-FEL project, he investigates the integration of plasma photocathodes into novel and state-of-the-art accelerators. he pioneered several conceptual breakthroughs that open the path towards ultra-compact plasma X-FELs, and awards recognized his work as an emerging researcher. His main research interests are generating the brightest electron beams from plasma-based accelerators for light sources, high-fields and high-energy physics applications.

Thomas Heinemann a research associate at the Heinrich Heine University Düsseldorf, Germany, has contributed crucially to the success of the E-210 experiment at SLAC FACET, as well as to the experimental realization of hybrid laser-plasma wakefield accelerators. The latter platform can be used to drive plasma photocathodes by electron beams from compact laser-wakefield accelerators, and thus allows plasma photocathodes to become ubiquitous. Thomas has received the Cockcroft Institute 2021 Early Career Excellence Award and is co-PI of the E-316: Icarus experiment at SLAC FACET-II.

Bernhard Hidding has invented the plasma photocathode, has led the E-210: Trojan Horse collaboration at FACET, which has demonstrated the first plasma photocathode, and leads the E-310: Trojan Horse-II collaboration at FACET-II. His ERC NeXource: Next-generation Plasma-based Electron Beam Sources for High-Brightness Photon Science project and the PWFA-FEL projects combine the generation of high-brightness beams from plasma-based accelerators with R&D towards their application. He is a professor at the Heinrich Heine University Düsseldorf, Germany, and a visiting professor at the University of Strathclyde, UK.